The Astrophysical Journal, 822:71 (20pp), 2016 May 10 doi:10.3847/0004-637X/822/2/71

A COLD FLARE WITH DELAYED HEATING

Gregory D. Fleishman[1,2], Valentin D. Pal'shin[2], Natalia Meshalkina[3], Alexandra L. Lysenko[2], Larisa K. Kashapova[3], and Alexander T. Altyntsev[3]
[1] Center For Solar-Terrestrial Research, New Jersey Institute of Technology, Newark, NJ 07102, USA
[2] Ioffe Institute, St. Petersburg 194021, Russia
[3] ISZF, Irkutsk, Russia
Received 2015 December 7; accepted 2016 March 22; published 2016 May 6

ABSTRACT

Recently, a number of peculiar flares have been reported that demonstrate significant nonthermal particle signatures with low, if any, thermal emission, which implies a close association of the observed emission with the primary energy release/electron acceleration region. This paper presents a flare that appears "cold" at the impulsive phase, while displaying delayed heating later on. Using hard X-ray data from Konus-*Wind*, microwave observations by SSRT, RSTN, NoRH, and NoRP, context observations, and three-dimensional modeling, we study the energy release, particle acceleration, and transport, and the relationships between the nonthermal and thermal signatures. The flaring process is found to involve the interaction between a small loop and a big loop with the accelerated particles divided roughly equally between them. Precipitation of the electrons from the small loop produced only a weak thermal response because the loop volume was small, while the electrons trapped in the big loop lost most of their energy in the coronal part of the loop, which resulted in coronal plasma heating but no or only weak chromospheric evaporation, and thus unusually weak soft X-ray emission. The energy losses of the fast electrons in the big tenuous loop were slow, which resulted in the observed delay of the plasma heating. We determined that the impulsively accelerated electron population had a beamed angular distribution in the direction of the electric force along the magnetic field of the small loop. The accelerated particle transport in the big loop was primarily mediated by turbulent waves, which is similar to other reported cold flares.

Key words: acceleration of particles – diffusion – magnetic fields – Sun: flares – Sun: radio radiation – turbulence

1. INTRODUCTION

The close causal relationship between nonthermal particles accelerated in flares due to the release of excessive magnetic energy and plasma heating has come to be known as the Neupert effect (Neupert 1968). Specifically, Neupert (1968) discovered that the soft X-ray (SXR) light curves in a number of flares during the rise phase and up to the SXR peak were well correlated with the running time integral of the impulsive microwave emission from the flare. Currently, the Neupert effect commonly refers to a similar relationship between the impulsive hard X-ray (HXR) and thermal SXR emissions. One way or the other, the Neupert effect suggests that (at least in some flares) particle acceleration takes place first, which gives rise to nonthermal microwave and HXR emission, and then the energy and momentum losses of these accelerated particles result in the thermal response in the form of coronal plasma heating and/or chromospheric evaporations; the heated coronal plasma then cools down relatively slowly due to conductive and radiative losses.

It was established long ago (e.g., Dennis 1988) that impulsive flares displaying a clear Neupert effect represent only a fraction of the total number of events. Most recently, using spectrally resolved X-ray data obtained with *Reuven Ramaty High Energy Solar Spectroscopic Imager* (*RHESSI*, Lin et al. 2002), many more low-energy, gradual (presumably, mostly thermal) events have been detected. For example, Su et al. (2008) find that about two-thirds of all events are gradual, up to 10% are impulsive, and up to 20% are early impulsive flares (Sui et al. 2006, 2007); only a fraction of the latter class of events demonstrates a clear Nuepert effect, which suggests that the relationships between nonthermal and thermal energies are generally much more complex (e.g., Veronig et al. 2005) than the simple loss-to-heating correspondence implied by the standard Neupert effect.

It has recently been recognized that some early impulsive flares are in fact "cold flares" (Bastian et al. 2007; Fleishman et al. 2011; Masuda et al. 2013) in which no or only a modest thermal plasma response is detected; these events are not listed as *GOES* flares. Three reported cold flares, although they are all similar in their lack of a thermal response, are, however, noticeably different from each other in a number of other respects. For example, the 2002 July 30 cold flare reported by Fleishman et al. (2011) is a "tenuous" flare with its thermal number density not exceeding 2×10^9 cm^{-3} at the coronal part of the flaring loop. In such cases, plasma heating due to fast electron collisions with coronal thermal particles is small because the collisions are rare in the tenuous plasma, while the chromospheric evaporation is suppressed for some reason. Contrary to this case, two other cold flares reported by Bastian et al. (2007) and Masuda et al. (2013) were dense with thermal number densities in excess of 10^{11} cm^{-3}. In such cases, the fast particle losses in the coronal part of the loop are large and the increase of the thermal energy is relatively strong; however, because of high density, the net temperature increase above the coronal preflare level is rather modest.

The Neupert effect is clearly present in the reported cold flares in its nominal form, i.e., the time derivative of the SXR light curve closely correlates with the light curves of the nonthermal HXR and microwave emissions. Morphologically, the microwave emission in all of the reported cold flares has a coronal (loop-like) structure, while the X-ray morphology differs depending on whether the flare is dense or tenuous: the dense flares demonstrate a coronal X-ray source, while the tenuous flare demonstrates two chromospheric foot points; the

coronal part of the cold flare sources has been identified with the acceleration region of the fast electrons (Fleishman et al. 2011). The timing of these events is inconsistent with the purely collisional transport of fast electrons, but instead requires the transport to be mediated by wave turbulence (Bastian et al. 2007; Fleishman et al. 2011). The spectra of fast electrons are typically hard in cold flares with a spectral index of $\delta \sim 3.5$. Overall, the cold flares appear to be events with efficient electron acceleration but only modest plasma heating. It appears that the heating is entirely supplied by energy loss of accelerated electrons without any apparent additional heating. Therefore, compared with other flare types, nonthermal-energy-dominated cold flares offer a cleaner way of studying electron acceleration in flares and their effect on the subsequent plasma heating. Thus, both the acceleration of electrons and non-thermal-to-thermal energy evolution can be studied much more conclusively in cold flares than in "normal" flares.

This paper presents the unusual case of a solar flare that shows only very mild thermal emission throughout the entire impulsive phase, similar to other cold flares, but then demonstrates more substantial heating which lasts considerably longer than the impulsive phase with a heating rate comparable to that observed in the impulsive phase. We argue that this behavior can be understood if two interacting loops are involved in the flare—a small loop and a large loop. The small loop, presumably in the region of its interaction with the big loop, plays the role of a particle accelerator and particle injector for the larger loop where the fast electrons are effectively accumulated. During the impulsive phase, the flare thermal response is driven by the fast electron losses from the small loop, but later it is driven by the same losses of the trapped population from the large loop. Based on X-ray and microwave data augmented by three-dimensional (3D) modeling, we estimate the key source parameters, such as the total number of nonthermal electrons, the spectral shape, and even the pitch-angle distributions in a few time frames. Also, we discuss the corresponding implications for particle acceleration, plasma heating, and thermal-to-nonthermal energy partitions.

2. OBSERVATIONS

2.1. Data Set Overview

The solar flare *GOES* class C5.1 occurred on 2002 March 10 near the eastern solar limb in AR 09866 (see the summary of the total power (TP) data in Figure 1). HXR and gamma-ray data for this event were obtained with the Konus-*Wind* (KW) spectrometer (Aptekar et al. 1995), while *RHESSI* (Lin et al. 2002) data were not available due to *RHESSI*'s night sequence.

KW is a joint US–Russian experiment launched on 1994 November 1 to study gamma-ray bursts and solar flares. It consists of two NaI(Tl) detectors S1 and S2 observing, respectively, the southern and northern celestial hemispheres. Unlike *RHESSI*, this instrument operates in interplanetary space (since 2004 near Lagrange point L1), so that it does not suffer from "nights," and thus has a very high duty cycle of about 95%. Thanks to being far from the Earth's magnetosphere it has an exceptionally stable background. KW works in two modes: waiting mode and trigger mode. In waiting mode, the count rate light curves are available in three wide energy channels, G1 (~18–70 keV), G2 (~70–300 keV), G3 (~300–1160 keV), with accumulation time 2.944 s. In trigger mode, KW measures count rate light curves in the same three channels with a varying time resolution from 2 to 256 ms and with a total duration of 230 s. While in trigger mode, 64 multichannel spectra are taken in addition to the light curves in the following manner. The multichannel spectra were measured in two partially overlapping energy bands, ~20–1200 keV and ~240 keV–15 MeV, in 2002. Each band has 63 energy channels with fixed nominal boundaries. The accumulation time of the first four spectra is fixed at 64 ms, and that of the last eight spectra at 8.192 s. For the remaining 52 spectra, the accumulation time is adaptively adjusted from 0.256 to 8.192 s

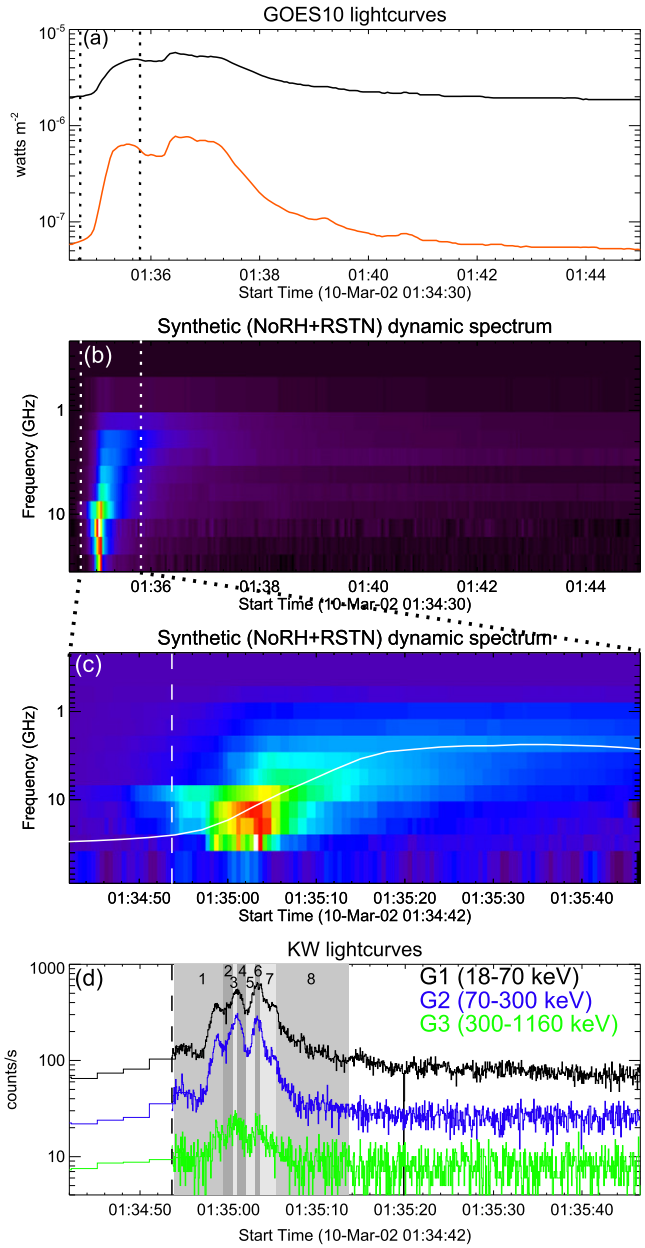

Figure 1. Overview of 2002 March 10 flare. (a) *GOES* (3 s) light curves as measured by *GOES-10*. (b) Microwave dynamic spectrum. (c) Zoom-in dynamic spectrum of the impulsive flare phase. White solid curve shows the high-energy *GOES* light curve. (d) Konus-*Wind* light curves in three energy bands. Dotted vertical lines in (a) and (b) denote the impulsive phase shown in panels (c) and (d). Dashed vertical lines in (c) and (d) show the start time of the Konus-*Wind* fast record. The vertical stripes shown by dark or light gray background denote the eight intervals over which we extracted the spectra in Figure 3.

based on the count rate in the G2 channel; for more intense events, the accumulation time is proportionally shorter. The trigger mode switches on at a statistically significant excess above a background count rate within an interval of 1 s or 140 ms in the G2 energy channel (Pal'shin et al. 2014).

The flare triggered the KW detector S2 at t_0(KW) = 5693.874 s UT (01:34:53.874). The propagation delay from *WIND* to the center of the Earth is 0.241 s for this flare[4]; the time corresponds to the Earth-crossing time of 01:34:54.115 UT.

Microwave TP data are obtained with the Nobeyama RadioPolarimeters (NoRP; Torii et al. 1979) in circular polarization at six frequencies (1, 2, 3.75, 9.4, 17, and 35 GHz) and in intensity only at 80 GHz with a time resolution of 0.1 s during the impulsive peak, 01:34:36–01:35:46 UT, and 1 s outside the peak (accordingly, no 80 GHz data); in addition, the intensity data from the Radio Solar Telescope Network (RSTN; Guidice et al. 1981) has 1 s time resolution at seven frequencies (0.4, 0.6, 1.4, 2.7, 5.0, 8.8, and 15.4 GHz).[5] The flux at 80 GHz was adjusted using the time-dependent correction coefficient $k_{\rm corr} = [T_{\rm years}/1995.83]^{630}$ (H. Nakajima 2007, private communication; see also Altyntsev et al. 2008; Kundu et al. 2009), while the polarizations at 1 and 2 GHz were corrected for differing gains in the I and V channels (K. Shibasaki 2007, private communication; see also Altyntsev et al. 2008). Using these heterogeneous sources of microwave data, we built two complementary dynamic spectra of the microwave burst. The first of them straightforwardly combines daily NoRP data with RSTN data, both of which have 1 s time (slow) resolution, to form a synthetic dynamic spectrum in the 0.4–35 GHz range. However, this dynamic spectrum is insufficient for our analysis for two reasons: during the impulsive peak, the emission (1) shows subsecond variations and (2) has a high-frequency spectral peak around 35 GHz. Thus, the fast NoRP record made in burst mode (0.1 s) containing the 80 GHz data is essential for this analysis.[6] We employ these high time resolution data in two ways. For the light curve and polarization data analysis, we use the full time resolution of 0.1 s. But for the spectral analysis, we also created a "fast" dynamic spectrum with 0.5 s resolution, which combines the NoRP 0.1 s data resampled to 0.5 s steps with interpolated (from 1 to 0.5 s) RSTN data. Adding the RSTN data, although it compromises the time resolution, is important for the spectral analysis because the NoRP data alone have too few data points to derive a meaningful spectral fit.

Microwave imaging was performed with the Siberian Solar Radio Telescope (SSRT) at 5.7 GHz (intensity and polarization) and the Nobeyama RadioHeliograph (NoRH, Nakajima et al. 1994) at 17 GHz (intensity and polarization) and 34 GHz (intensity only). The SSRT is a cross-shaped interferometer and the data recorded by the EW and NS arrays provide two-dimensional (2D) images of the solar disk every two to three minutes and one-dimensional (1D) images every 0.3 s in the standard mode of observation (Grechnev et al. 2003). The methods of analysis for one-dimensional solar images have been described by Altyntsev et al. (2003) and Lesovoi & Kardapolova (2003). The SSRT receiver system contains a spectrum analyzer with frequency coverage of 120 MHz using an acousto-optic detector with 250 frequency channels, which correspond to the knife-edge-shaped fan beams for the NS and EW arrays. The frequency channel bandwidth is 0.52 MHz. The response at each frequency corresponds to emission from a narrow strip on the solar disk whose position and width depend on the observation time, array type, and frequency. The signals from all of the channels are recorded simultaneously and generate a one-dimensional distribution of solar radio brightness. During the event under study, the width of the beam of SSRT was 18″ for the EW array and 30″ for the NS array.

Limited information about the thermal plasma at the flare region is available from a few images taken at 195 Å with the Extreme ultraviolet Imaging Telescope (EIT) on board the *Solar and Heliospheric Observatory* (*SoHO*/EIT; Domingo et al. 1995) with 12 minute cadence. The context SXR *GOES-10* data and the line-of-sight magnetogram from the Michelson Doppler Imager (*SoHO*/MDI; Domingo et al. 1995) are utilized. The line-of-sight magnetogram is used for 3D modeling with the GX Simulator (Nita et al. 2015).

2.2. Light Curves

A striking feature of this flare is the contrasting combination of the impulsive and gradual light curves, which is vividly illustrated in Figure 2. Prominent impulsive emission is apparent in the KW light curves and in the high-frequency microwave light curve at 35 GHz, while the microwave light curves become progressively more gradual toward lower frequencies; the *GOES* light curves are even more gradual than the low-frequency microwave light curves. Thus, this section pays close attention to these various light curves and the relationships between them.

Figure 2(a) shows the general similarity between the microwave light curve at 35 GHz, the HXR KW G2 light curve at 70–300 keV, and the time derivative of the microwave light curve at 3.75 GHz. Although these three light curves differ from each other in some details, the overall high correlation between them is apparent; no delay is seen between the light curves.

Figure 2(b) compares the high-energy KW channels G2 and G3 with the high-frequency microwave 35 and 80 GHz light curves over the impulsive phase of the burst. The 35 GHz light curve correlates as closely with each of the HXR light curves as the HXR light curves correlate with each other. Again, no delay between the 35 GHz and HXR light curves is apparent within the instrumental time resolution (64 ms in case of KW and 100 ms in case of NoRP). On the contrary, the 80 GHz light curve does not correlate in detail with all of the other light curves, which is the result of the previously mentioned 4 s smoothing of the 80 GHz light curve needed to reduce the high fluctuation level in the original signal. Figure 2(c) displays a similar relationship, but between the KW G2 light curve and the microwave light curves at 17 and 9.4 GHz. In this case, the microwave light curves are less impulsive than and delayed relative to the HXR light curve, while the shapes of the microwave light curves at 9.4 and 17 GHz are closely correlated with each other at the rise phase, where they appear earlier than the most impulsive light curves.

Figure 2(d) compares, in the first place, the impulsive 35 GHz light curve and the derivative of the GOES(1–8 Å) light curve. In contrast to the expectation based on the

[4] The corresponding delay to the Nobeyama Observatory whose microwave data are used for the analysis is 0.231 s.

[5] To correct for RSTN clock and amplitude calibration errors, the RSTN time was shifted as $t_{\rm true} = t_{\rm obs} - 3.3$ s; the light curve at 8.8 GHz was corrected by a factor of 1.4 and at 15.4 GHz by a factor of 1.55.

[6] The original 80 GHz data are very noisy; they were smoothed using a 4 s window before inclusion in the dynamic spectrum.

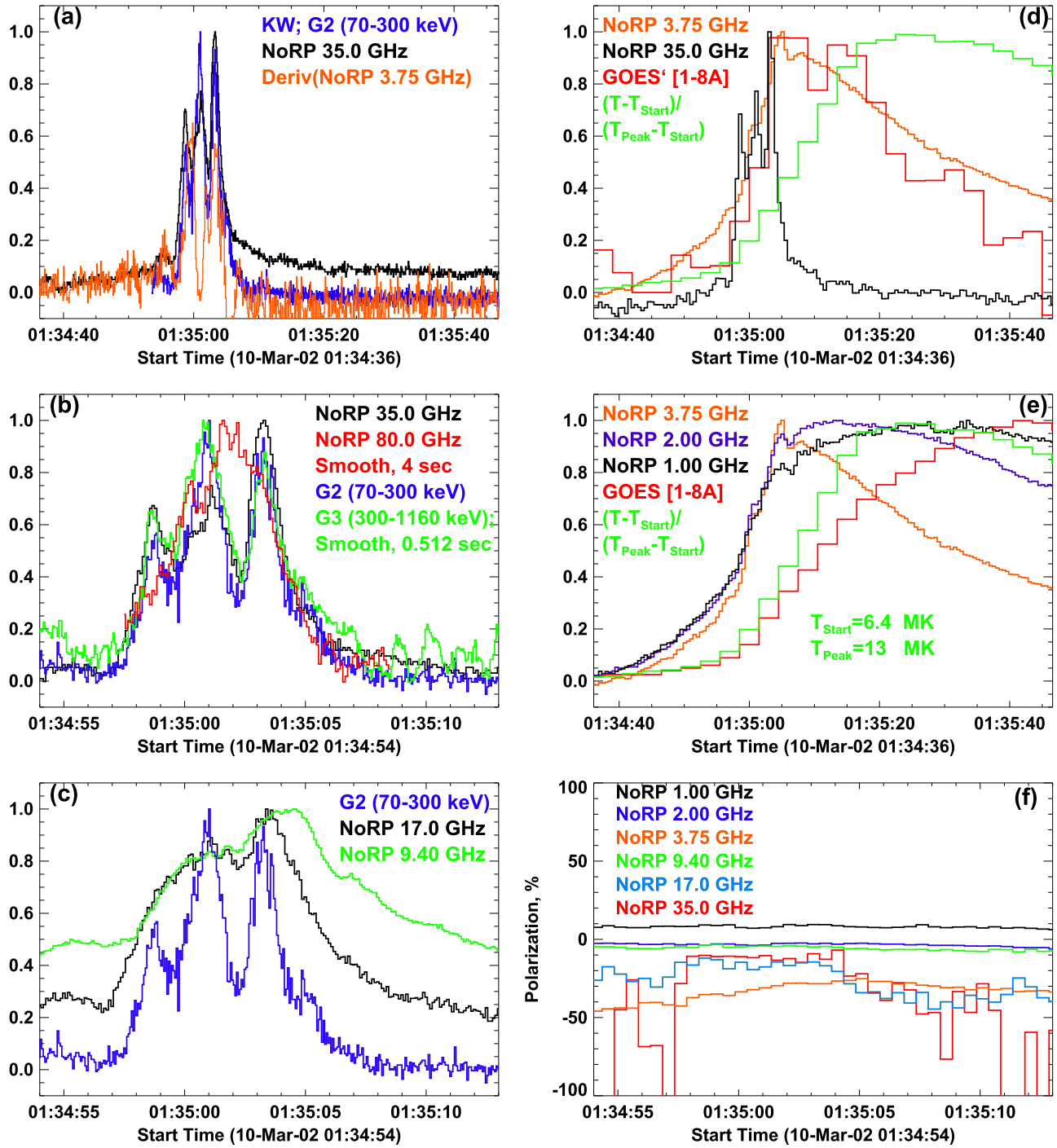

Figure 2. Summary of the normalized light curves. (a) Overall comparison of the impulsive microwave and HXR light curves at 35 GHz (0.1 s cadence) and 70–300 keV (64 ms cadence) with the time derivative of the gradual microwave light curve at 3.75 GHz. (b) Microwave light curves at 35 and 80 GHz along with Konus-*Wind* HXR G2 and G3 light curves. (c) Microwave light curves at 9.4 and 17 GHz compared with Konus-*Wind* HXR G2 light curve. (d) Microwave light curves at 3.75 and 35 GHz along with time derivative of the GOES(1–8 Å) light curve and *GOES*-derived plasma temperature evolution ($T_{\rm Start} \approx 6.4$ MK; $T_{\rm Peak} \approx 13$ MK). (e) Microwave light curves at 1, 2, and 3.75 GHz along with GOES(1–8 Å) light curve and *GOES*-derived plasma temperature. (f) The degree of polarization of the microwave emission at the impulsive flare phase. Note the increase of the degree of polarization at 17 and 35 GHz at the decay phase.

standard Neupert effect, these two light curves do not correlate with each other: even though the *GOES* derivative does reach the peak value at the impulsive peak, it appears strongly delayed relative to the impulsive light curve. For further reference, this panel also displays the *GOES*-derived evolution of the plasma temperature and a more gradual microwave light curve at 3.75 GHz, which shows a much closer correlation with the *GOES* derivative. Then, Figure 2(e) displays all of the gradual low-frequency microwave light curves, the GOES(1–8 Å) light curve, and the temperature evolution. This comparison shows that the light curves are becoming more and more gradual and delayed at lower frequencies, with the *GOES* light curve being the most delayed. This delay, even though its absolute value

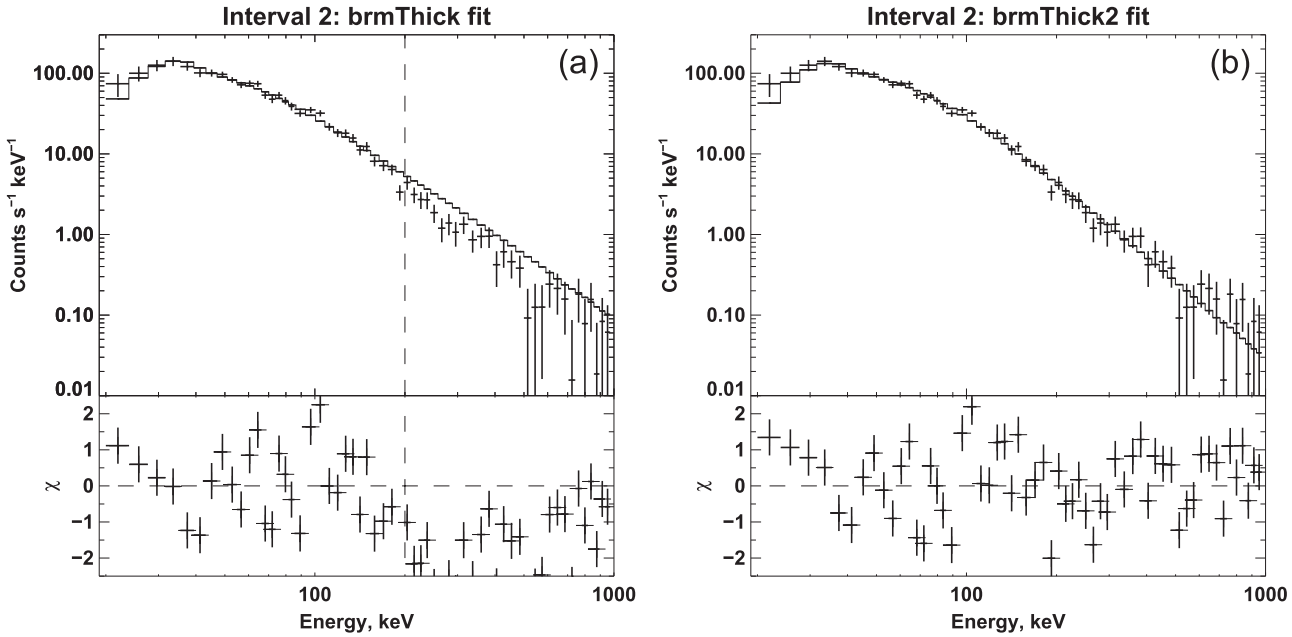

Figure 3. Konus-*Wind* spectrum of the flare for time interval #2 (Figure 1(d)) with the fit examples: (a) brmThick model fit to the photon energy range 20–200 keV denoted by the vertical dashed line, (b) brmThick2 model fitted to the full range of 20–1000 keV.

appears small (about 40 s), is highly substantial, indicating a heating process that is roughly four times longer than the duration of the impulsive phase. The temperature light curve is well correlated with the 1 GHz light curve at the peak phase. It is interesting to recall here (Figure 2(a)) that the impulsive 35 GHz and HXR light curves are well correlated with the time derivative of the 3.75 GHz light curve (rather than the SXR light curve). This correlation indicates that the 3.75 GHz light curve either represents the plasma thermal response on the accelerated electron impact or corresponds to a trapped population of fast electrons, whose injection profile corresponds to the 35 GHz or KW light curves.

Figure 2(f) shows evolution of the degree of polarization of the microwave emission during the impulsive peak. Two interesting features are to be noted about this figure: (i) an unexpectedly high degree of polarization at 3.75 GHz during the entire event[7], indicating optically thin emission at these intermediate frequencies, and (ii) the degree of polarization at 17 and 35 GHz is becoming larger during the decay of the impulsive phase, which may imply substantial modification of the angular distribution of the nonthermal electrons; we return to these points later.

2.3. Spectra

2.3.1. X-Ray Spectra

We performed analysis of the KW spectral data for the eight time intervals indicated in Figure 1(d) where the signal exceeded the background. For the analysis, the energy channels were rebinned to contain at least 20 counts per energy bin in each time interval and fit in various energy subranges within the 20–1000 keV range, as detailed below. Although the emission is seen up to ∼10 MeV, we did not include the channels above 1 MeV since they can contain a significant contribution from nuclear line emission, which is not discussed here.

We fit the spectra with a number of alternative spectral models. Unambiguously, a single power law (either of the electron or photon spectra) is inconsistent with the data when the whole range of photon energies, 20–1000 keV, is analyzed. On the other hand, when a broken power-law model is applied for the either electron or photon spectrum, the fit parameters are returned with rather large uncertainties, which implies that a wide range of spectral models is consistent with the data. In particular, a single power law can fit the data reasonably well when a truncated photon energy range is selected, e.g., 20–200 keV (Figure 3(a)), 40–400 keV, or 100–1000 keV, which may imply that spectral steepening progresses slowly but steadily with energy. A number of instrumental or physical effects are known to yield spectral flattening at low energies, namely, photon pile-up, photospheric albedo, nonuniform ionization of the target, and return current. We checked via modeling that pile-up plays no role in our case. The other effects which we noted typically play a role at low energies, $E \lesssim 50$ keV (Holman et al. 2011), while in our flare the spectral break happens at much higher energy $E \gtrsim 100$ keV. Nevertheless, we employed the fit with albedo correction, but this did not improve the goodness of fit. Also, we superimposed a thermal bremsstrahlung model with a temperature of ∼14 MK and an emission measure (EW) of $\sim 2 \times 10^{48}$ cm^{-3}, as estimated from the *GOES* peak flux on our spectra, and found that the thermal contribution does not exceed 1% even at the lowest energy channels. As a result of our tests, we conclude that the nonthermal electron spectrum has a convex shape (the high-energy slope is steeper than the low-energy one). Out of the variety of spectral models considered, here we present some results for three models using XSPEC 12.5 (Arnaud 1996).

[7] A comparably strong polarization (not shown in the figure) is detected at 5.7 GHz with SSRT.

The first model is a phenomenological broken power-law model (BPL) which takes the form

$$I(E) = \begin{cases} A\left(\frac{E}{100\,\mathrm{keV}}\right)^{-\gamma_1} & E \leqslant E_{\mathrm{br,ph}} \\ AE_{\mathrm{br,ph}}^{\gamma_2-\gamma_1}\left(\frac{E}{100\,\mathrm{keV}}\right)^{-\gamma_2} & E_{\mathrm{br,ph}} < E, \end{cases} \quad (1)$$

where γ_1 and γ_2 are the *PL photon* indexes and A is the normalization at 100 keV in units of photons $\mathrm{cm}^{-2}\,\mathrm{s}^{-1}\,\mathrm{keV}^{-1}$.

The other two models are collisional thick-target models assuming a power law (brmThick) in the fast electron flux spectrum (el's/keV/s) over energies between the low- and high-energy cutoffs,

$$F(E) = \begin{cases} 0 & E < E_{\mathrm{cut,low}} \\ \propto E^{-\delta} & E_{\mathrm{cut,low}} \leqslant E \leqslant E_{\mathrm{cut,high}} \\ 0 & E_{\mathrm{cut,high}} < E, \end{cases} \quad (2)$$

and a broken power-law electron spectrum (brmThick2),

$$F(E) = \begin{cases} 0 & E < E_{\mathrm{cut,low}} \\ \propto E^{-\delta_1} & E_{\mathrm{cut,low}} \leqslant E \leqslant E_{\mathrm{br},e} \\ \propto E^{-\delta_2} & E_{\mathrm{br},e} \leqslant E \leqslant E_{\mathrm{cut,high}} \\ 0 & E > E_{\mathrm{cut,high}}, \end{cases} \quad (3)$$

normalized to the total flux of the electrons (electrons s^{-1}) above $E_{\mathrm{cut,low}}$. Since the XSPEC package does not contain standard models of the thin or thick targets from a broken power-law distribution of the nonthermal electrons, as are routinely used for the analysis of the X-ray spectra of solar flares, we added these models to XSPEC based on analogous models used in the OSPEX package (Schwartz et al. 2002). We also performed the corresponding fit using the OSPEX package from SSW/IDL to cross-check the fit results and found that the fit parameters are fully consistent with each other.

Given that the *GOES* flux was somewhat low during the impulsive flare phase, we examined whether or not the *GOES* data can constrain the low-energy cut-off in the accelerated electron spectrum. However, no conclusive constraint was obtained, perhaps because of a mild thermal emission contribution at the *GOES* range. Accordingly, the low-energy cut-off was fixed to 10 keV (i.e., below the KW fitting range). The mean atomic number of the target plasma, Z, was set to 1.2 to account for the contribution from target nuclei heavier than hydrogen.

The fit examples are given in Figure 3, while the fit results are summarized in Figure 4 and in Table 1 (the errors are given at the 68% confidence level). The fact that the HXR spectral analysis could only be performed for a few uneven time intervals, #1–8 indicated in Figure 1(d), complicates the study of the spectral evolution and the comparison with microwave spectral data. However, if the actual electron spectrum does not deviate strongly from a single power law, then the effective spectral slope can be estimated from the hardness ratio, which is the ratio of X-ray fluxes recorded in two adjacent, wide energy ranges, G1 and G2, or G2 and G3. To this end, we fit the spectra in our eight available intervals with a single power law (brmThick) at the photon energy range 20–200 keV and then cross-correlated the obtained spectral index δ with the hardness ratio HR_{21}. Figure 4(a) shows that these two values demonstrate excellent correlation and reveal the following regression law:

$$\delta = 2.7 - 1.93 \log \mathrm{HR}_{21}, \quad (4)$$

and thus the spectral evolution in this energy range can be recovered with a very high cadence; since the spectral hardness data are available with very high time resolution (down to 16 ms), the δ time evolution can be recovered with a comparably high time resolution. We searched for but did not find any significant variation of the spectral index δ on timescales much shorter than 1 s, and thus we derived the δ evolution with the 0.5 s cadence needed for comparison with the microwave spectral fit results available with the same cadence.

As has been said, the single power law does not fit the data well over the entire range 20–1000 keV; therefore, we used a broken power law over either photon or electron energy. We found that the results of the fit to the bands, photon broken power law (BPL) are more stable compared to the fit to the bands, electron broken power law (brmThick2); in the latter case, the confidence interval of the fit parameters appears to be rather broad if all of the parameters of the broken power law are kept free, especially for intervals 4–7 (again, we are referring to Figure 1(d)), while interval 8 can, in fact, be fit by a single power-law model. This behavior of the fit implies that the change of the spectral slope is modest and likely gradual, and so no exact value of the break energy could be identified from the data. To obtain a more stable fit result for intervals 4–7, we first fixed the high-energy slope δ_2 to the values implied by the BPL fits ($\delta_2 = \gamma_2 + 1$) and determined the break energies in the electron spectrum. Then, we cross-correlated the break energies in these two fits, BPL and brmThick2, to determine a regression law between them (Figure 4(b)). In the next step, we fixed the break energies at the values implied by this regression law and fit the spectra with free spectral indices. The results of these slightly different versions of the brmThick2 fits agree well with each other, which confirms that the spectral model with a broken power law is overall consistent with the data.

The remaining panels of Figure 4 display correlation plots between the different pairs of spectral indices obtained from the fits. Figures 4(c) and (d) show correlation plots between the low- and high-energy spectral indices. The results are somewhat different between the BPL and brmThick2 fits. Although γ_1 and γ_2 show a significant correlation for the BPL fit, the correlation between δ_1 and δ_2 is barely visible, implying that the low- and high-energy slopes in the spectrum of nonthermal electrons are independent. If so, then the correlation between γ_1 and γ_2 can be understood as the result of some contribution of high-energy electrons to the low-energy photon spectrum.

The classical thick-target model (Brown 1971; Somov & Syrovatskiĭ 1976) implies a simple, unique relationship between the photon and electron spectral indices, $\delta = \gamma + 1$. However, one should note that the numbers in Table 1 do not follow this simple formula because additional physical processes are included in brmThick2 model and also because of the potential complexity of the spectrum, which is not captured by the simplified models. The two bottom panels of Figure 4 display the correlation plots between the low-energy (γ_1 and δ_1) and high-energy (γ_2 and δ_2) spectral indices, respectively. In both cases, there is a significant correlation, which, however, noticeably deviates from the expectation based on the classical thick-target emission model.

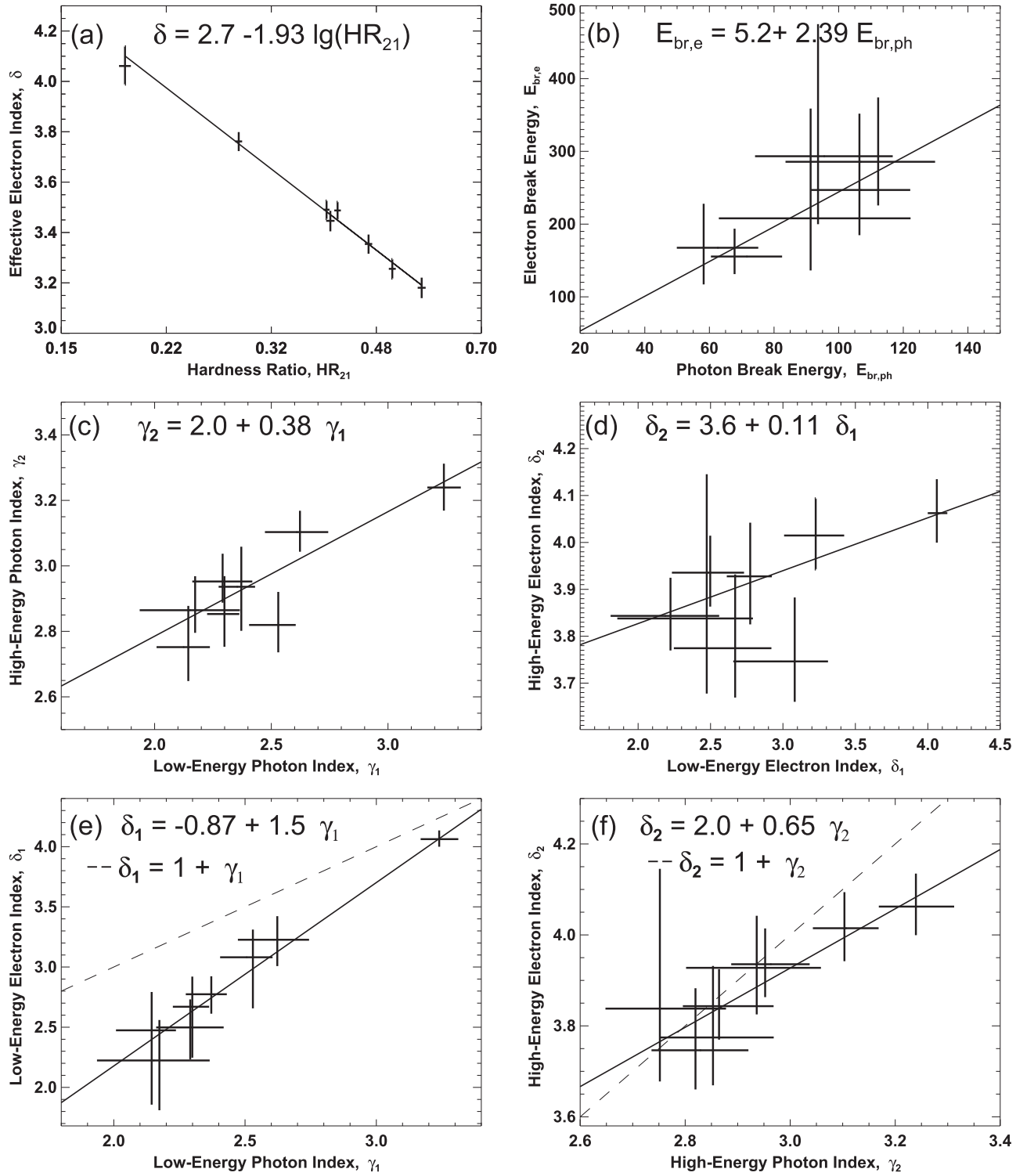

Figure 4. Correlation plots for the HXR fit parameters. (a) Cross-correlation between effective power-law index of electron distribution δ, derived from the brmThick fit, Equation (2), and hardness ratio HR_{21} for the eight analyzed spectra; (b) cross-correlation between the break energies in the photon and electron fits; (c) cross-correlation between the low- and high-energy photon indices $\gamma_{1,2}$; (d) cross-correlation between the low- and high-energy electron indices $\delta_{1,2}$; (e) cross-correlation between the photon and electron low-energy indices γ_1 and δ_1; (f) cross-correlation between the photon and electron high-energy indices γ_2 and δ_2. The dashed lines in (e) and (f) show simple expectations based on classical thick-target model $\delta = \gamma + 1$.

Interestingly, for the high-energy spectral indices, the regression curve is shallower than $\delta_2 = \gamma_2 + 1$ (dashed line), although most of the index pairs are quantitatively consistent with the expectation of $\delta_2 = \gamma_2 + 1$. In contrast, for the low-energy indices, the regression is steeper and does not cross the data points at all, which can again be interpreted in terms of the contribution from the high-energy electrons to the lower-energy X-ray emission.

The spectra are hard over the entire considered energy range. The low-energy part of the spectrum shows $\gamma_1 \sim 2$–3.3 and δ_1

Table 1
Summary of the Konus-*Wind* Spectral Fits (20 keV–1 MeV)

			BPL						brmThick2				
No.	$T_{\rm start}$[a] (s)	ΔT (s)	γ_1	γ_2	$E_{\rm br,\ ph}$ (keV)	A[b]	Flux[c]	χ^2/dof	δ_1	δ_2	$E_{\rm br,\ e}$ (keV)	Electron Flux[d]	χ^2/dof
1	0.000	5.632	$2.53^{+0.08}_{-0.12}$	$2.82^{+0.10}_{-0.08}$	91^{+30}_{-28}	$0.079^{+0.008}_{-0.004}$	$4.48^{+0.13}_{-0.13}$	0.67(36.7/55)	$3.08^{+0.23}_{-0.42}$	$3.75^{+0.14}_{-0.09}$	208^{+151}_{-72}	$1.0^{+0.6}_{-0.5}$	0.66(36.5/55)
2	5.632	1.024	$2.30^{+0.06}_{-0.07}$	$2.85^{+0.11}_{-0.10}$	106^{+15}_{-15}	$0.268^{+0.014}_{-0.011}$	$13.3^{+0.3}_{-0.3}$	0.86(47.4/55)	$2.67^{+0.25}_{-0.42}$	$3.77^{+0.16}_{-0.11}$	247^{+105}_{-62}	$1.1^{+0.8}_{-0.6}$	0.92(50.6/55)
3	6.656	0.512	$2.14^{+0.09}_{-0.14}$	$2.75^{+0.13}_{-0.10}$	94^{+23}_{-19}	$0.424^{+0.048}_{-0.028}$	$19.5^{+0.5}_{-0.5}$	0.82(29.4/36)	$2.47^{+0.32}_{-0.62}$	$3.84^{+0.31}_{-0.16}$	293^{+182}_{-93}	$1.0^{+0.9}_{-0.6}$	0.84(30.2/36)
4	7.168	1.024	$2.37^{+0.06}_{-0.10}$	$2.94^{+0.12}_{-0.13}$	112^{+17}_{-29}	$0.232^{+0.017}_{-0.009}$	$11.9^{+0.3}_{-0.3}$	1.1(60.5/55)	$2.77^{+0.15}_{-0.16}$	$3.93^{+0.11}_{-0.10}$	282[e]	$1.3^{+0.5}_{-0.4}$	1.1(61.0/56)
5	8.192	1.024	$2.29^{+0.13}_{-0.13}$	$2.95^{+0.08}_{-0.06}$	68^{+14}_{-7}	$0.33^{+0.04}_{-0.03}$	$14.6^{+0.4}_{-0.4}$	0.87(47.8/55)	$2.50^{+0.23}_{-0.26}$	$3.94^{+0.08}_{-0.07}$	169[e]	$1.3^{+0.7}_{-0.5}$	0.88(49.2/56)
6	9.216	0.512	$2.17^{+0.19}_{-0.24}$	$2.86^{+0.10}_{-0.07}$	58^{+17}_{-8}	$0.48^{+0.12}_{-0.08}$	$18.8^{+0.6}_{-0.6}$	0.71(24.8/35)	$2.2^{+0.3}_{-0.4}$	$3.84^{+0.08}_{-0.07}$	144[e]	$1.1^{+0.9}_{-0.5}$	0.72(26.0/36)
7	9.728	1.792	$2.62^{+0.12}_{-0.15}$	$3.10^{+0.07}_{-0.06}$	58^{+8}_{-7}	$0.186^{+0.027}_{-0.018}$	$9.9^{+0.3}_{-0.3}$	1.15(47.0/41)	$3.23^{+0.20}_{-0.22}$	$4.01^{+0.03}_{-0.07}$	144[e]	$4.3^{+2.0}_{-1.5}$	1.12(47.1/42)
8[f]	11.520	8.192	$3.24^{+0.07}_{-0.07}$	$3.24^{+0.07}_{-0.07}$	⋯	$0.0200^{+0.0010}_{-0.0010}$	$2.21^{+0.20}_{-0.20}$	0.82(46.8/57)	$4.07^{+0.07}_{-0.07}$	$4.07^{+0.07}_{-0.07}$	⋯	$4.1^{+0.8}_{-0.6}$	0.81(46.4/57)

Notes.
[a] Since t_0(KW) = 5694.105 s UT (01:34:54.105).
[b] In units of photons cm^{-2} s^{-1} keV^{-1}.
[c] In units of 10^{-6} erg cm^{-2} s^{-1} in energy range 20–1000 keV.
[d] In units of 10^{35} electrons s^{-1}.
[e] Fit with frozen $E_{\rm br,\ e}$.
[f] Fit by a single power law.

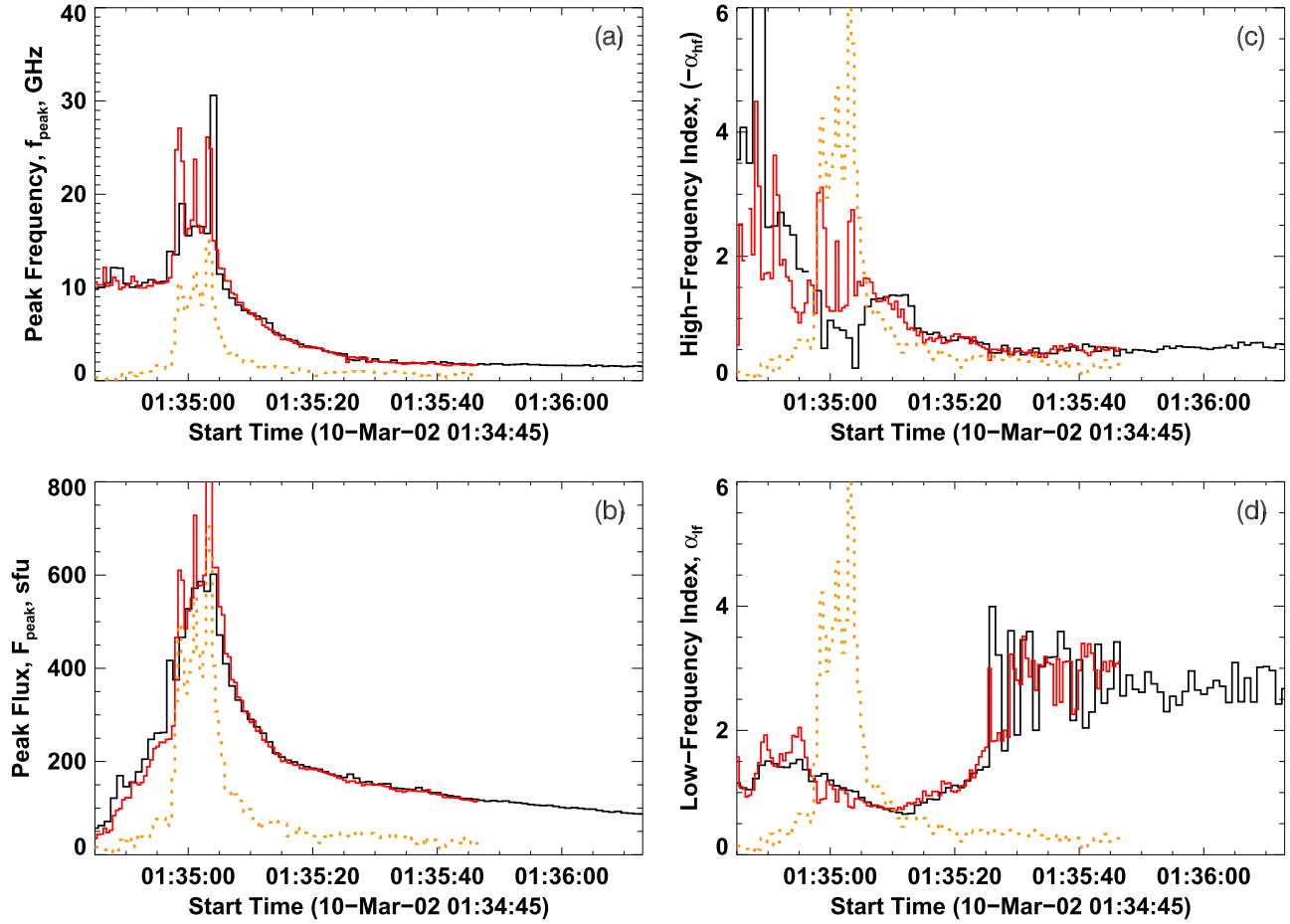

Figure 5. Microwave spectral fit parameter evolution: black curves are from 1 s data, red curves are from 0.5 s data, and the dotted orange curves are the appropriately scaled light curve at 35 GHz. (a) Peak frequency evolution. (b) Peak flux evolution. (c) Evolution of high-frequency spectral index. (d) Evolution of low-frequency spectral index.

$\sim$ 2–4. The steeper, high-energy spectra are still hard with $\gamma_2 \sim$ 2.7–3.3 and $\delta_2 \sim$ 3.7–4.1. The fluence of the flare measured from 01:34:54.105 UT to 01:35:13.817 UT is $(1.214 \pm 0.020) \times 10^{-4}$ erg cm^{-2} and the 64 ms peak flux measured from 01:35:00.761 UT to 01:35:01.273 UT is $(1.95 \pm 0.05) \times 10^{-5}$ erg cm^{-2} s^{-1} (both in the 20–1000 keV range). Assuming isotropic emission, the corresponding radiated X-ray energy is $(3.36 \pm 0.06) \times 10^{23}$ erg and the peak HXR luminosity is $(5.40 \pm 0.13) \times 10^{22}$ erg s^{-1}.

2.3.2. Microwave Spectra

To obtain the microwave spectral evolution, we employed two synthetic dynamic spectra, "slow" (Figure 1(b)) and "fast" (Figure 1(c)), described in Section 2.1. The slow dynamic spectrum allows for longer tracking of the burst evolution, while the fast one has the advantage of a better time resolution and 80 GHz data which generally help to better constrain the high-frequency spectral slope. It has to be kept in mind, however, that if the spectral peak is too high ($\sim$35 GHz) and the high-frequency slope is only constrained by the 4 s smoothing of the poorly defined 80 GHz data point (see Figure 2(c)), then the value of the high-frequency microwave spectral index could not be reliably determined.

Both the slow and fast dynamic spectra were sequentially fit with the so-called microwave generic function proposed by Stahli et al. (1989):

$$S = e^{A} f^{\alpha} [1 - e^{-e^{B} f^{-\beta}}], \quad (5)$$

where f is the frequency in GHz, and A, B, α, and β are the free fitting parameters from which the relevant spectral parameters are computed. Specifically, the low-frequency spectral index $\alpha_{\rm lf} \equiv \alpha$, while the high-frequency spectral index is $\alpha_{\rm hf} = \alpha - \beta$. The peak frequency and the flux density at peak frequency are calculated from the shape of function S as described by Nita et al. (2004). Following Nita et al. (2004), we used the corresponding built-in functionality of the `ovsa_explorer` widget from the OVSA software available from the SSW distribution.

Figure 5 shows a summary of the microwave spectral fit. The fit results obtained from the slow and fast dynamic spectra generally agree with each other, but nevertheless show a number of mismatches; most notably during the highly impulsive peak phase. The peak flux and peak frequency determined from the fast dynamic spectrum display a significantly stronger variation than the slow ones, which is real and reflects the actual subsecond impulsiveness of the burst. On the other hand, the corresponding strong variations of the "fast" high-frequency spectral index are not real: they only take place when the spectral peak frequency is about 35 GHz,

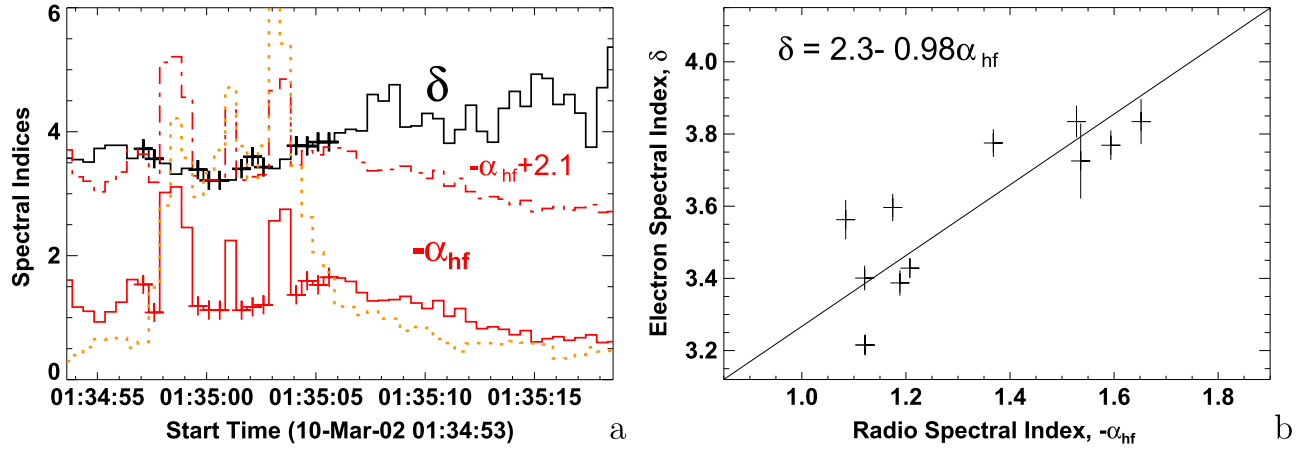

Figure 6. Comparison between the microwave and HXR spectral indices. (a) Evolution of the electron flux spectral index δ (black curve) derived from the spectral hardness, as explained in Section 2.3.1, and microwave high-frequency spectral index $\alpha_{\rm hf}$ (red curve). The red dashed–dotted curve shows the same microwave spectral index but displaced by 2.1 upward to ease visual comparison with the HXR-derived electron spectral index. The plus symbols show the data points used for correlation analysis during the impulsive flare phase, which is depicted by the 35 GHz light curve shown with the orange dotted curve. (b) The scatter plot of the indices and the corresponding linear fit.

so that the high-frequency slope is only constrained by poorly known 80 GHz data, as pointed out above.

There are a number of properties of the fit parameter evolution which are worth mentioning. The spectral peak frequency demonstrates a remarkably large variation by far more than an order of magnitude: around 10 GHz at the burst rise phase, then up to at least 35 GHz during the peak phase, and finally down to roughly 1.5 GHz at the decay phase. Thus, the entire range of the spectral peak variation is within a factor larger than 20, which is a substantially broader range than for a "typical" microwave burst (Nita et al. 2004; Melnikov et al. 2008). This observation alone is strong evidence that the magnetic field at the radio source at the decay phase is much smaller than that at the peak phase; see Section 3.1 for details. Although there is an overall correspondence between the spectral peak flux and peak frequency in the sense that the larger the flux the larger the peak frequency, there is no perfect correlation between these two parameters. Indeed, if we compare the rise and decay phases, we note immediately that the same peak flux corresponds to substantially smaller peak frequency at the decay than at the rise phase. Note, also, that at the early decay phase, the peak flux and frequency decline highly consistently with each other, but after roughly 01:35:30 UT the decrease of the peak frequency terminates while the peak flux continues to decline.

The high- and low-frequency spectral indices also display substantial evolution. At the rise, peak[8], and early decay phases, the high-frequency spectral index shows a soft–hard–soft (SHS) pattern similar to that often reported for HXR spectra. However, around 01:35:10 UT, the softening terminates and again gives way to spectral hardening. This hardening continues until 01:35:30 UT, when $\alpha_{\rm hf}$ hits the level of $\alpha_{\rm hf} \approx -1$ and then stays roughly constant. The low-frequency spectral index decreases all the way during the rise, peak, and early decay phases until roughly 01:35:10 UT, and then turns to increase until 01:35:30 UT, when it hits the level of $\alpha_{\rm lf} \approx 3$. After that point, it remains approximately constant at this level until the end of the event. Overall, the event demonstrates a strikingly prominent spectral variability over the rise, peak, and early decay phases (until ~01:35:30 UT), but shows no spectral evolution after that.

[8] Neglecting the three outliers during the three most impulsive peaks.

2.3.3. Comparison of the X-Ray and Microwave Spectral Indices

As we have both HXR and microwave spectral fits, it is reasonable to compare the "effective" spectral index δ of the electron flux derived from the HXR hardness ratio with Equation (4) and the high-frequency microwave spectral index $\alpha_{\rm hf}$ primarily defined by the energy spectrum of the fast electron number density in the source of the microwave emission. Figure 6(a) shows that these spectral indices evolve consistently over the impulsive phase of the event, as marked on the δ curve by plus signs outside the mentioned outliers. Both spectral indices show the SHS evolution, while they tend to disagree outside of the impulsive peak. In spite of this apparent consistency, the scatter plot of the spectral indices during the impulsive phase displays no perfect correlation (Figure 6(b)), although the data points roughly follow the linear regression law $\delta \approx 2.3 - 0.98\alpha_{\rm hf}$.

2.4. Imaging

A summary of the imaging data is given in Figure 7. The background color in Figure 7, left, shows one of the two 195 Å EIT/*SOHO* difference images[9] on which a representative set of microwave contours is superimposed along with the relevant neutral lines obtained from the *SoHO*/MDI photospheric magnetogram.

The difference image demonstrates the presence of two bright, compact kernels at the flare time separated by about 10″ in the north–south direction, which are not seen 12 minutes apart either before or after the flare. Microwave images at 17 and 34 GHz also show a double source structure but with a much larger separation between the sources, roughly 85″. It is interesting that the EUV kernels are co-located with the strongest, i.e., southern, microwave source; the northern kernel spatially coincides with the centroid of the microwave source at the impulsive flare phase. There are two magnetic neutral lines;

[9] Three 195 Å images were available taken on 01:25:52.555 UT, 01:36:14.749 UT, and 01:48:06.640 UT.

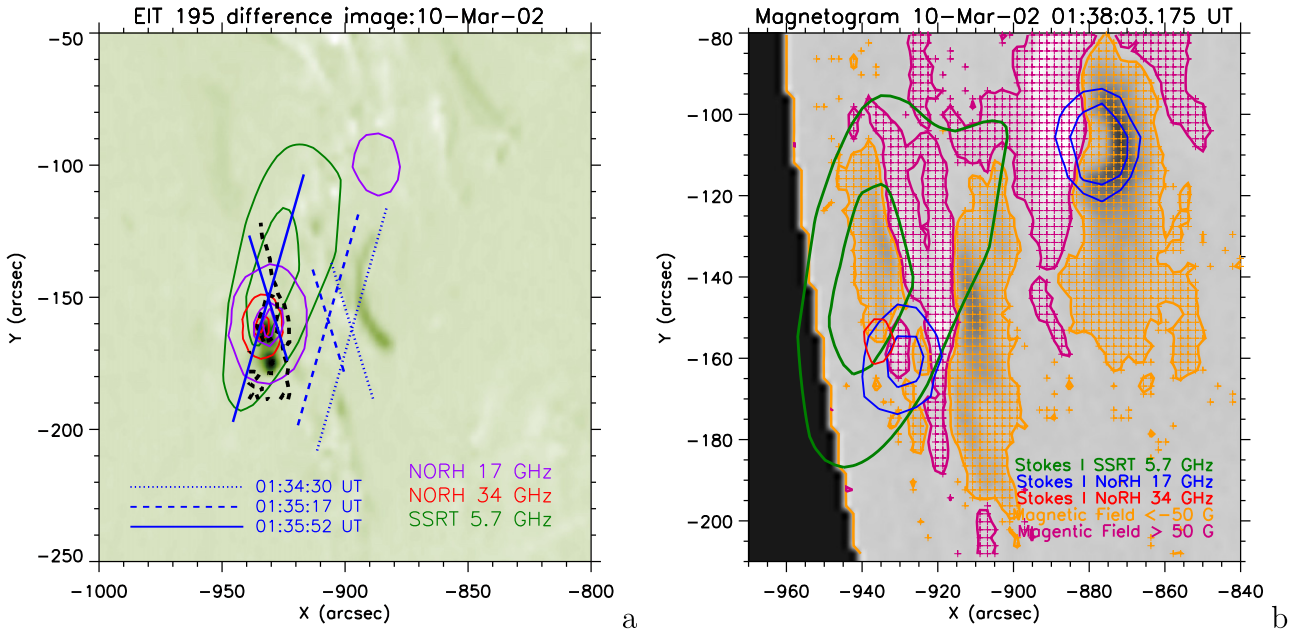

Figure 7. (a) The 195 Å EIT/*SOHO* difference negative image between 01:36:14.7490 UT and 01:25:52.555 UT. Contours show microwave images at 34 GHz (red) and 17 GHz (violet) obtained at 01:35:01 UT by NoRH with intensity levels at 20% and 70% of the maximum. Green contours show 5.7 GHz image obtained by SSRT at 01:37:11 UT with intensity levels 70% and 90% of maximum. The dashed black line shows several neutral lines taken from photospheric magnetogram by MDI/*SOHO*. Intersections of the blue cross bars (dotted, dashed, and solid) present centroids of 5.7 GHz source at different moments. The direction of each cross bar shows the scanning direction of either EW or NS array. The length of each cross bar indicates the source width at half maximum over this bar direction. (b) *SoHO*/MDI magnetogram, where the locus of pixels with $B_{\|} > 50$ G is shown in magenta, while with $B_{\|} < -50$ G is shown in orange. Contours of the microwave emission at 5.7, 17, and 34 GHz are shown for the decay phase.

the shorter one separates the EUV kernels, while the longer one separates the microwave sources. These relationships imply that magnetic connectivity is possible both between the EUV kernels and between the microwave sources.

The positions of the 17 and 34 GHz sources do not change over the course of the flare. During the impulsive phase, the southern source dominates at both 17 and 34 GHz (Figure 7), while during the decay phase the brightness of these two sources is comparable at 17 GHz; however, the northern source is not seen at all at 34 GHz. Both microwave sources produce left circular polarization (LCP) at 17 GHz. Remarkably (Figure 8), the Northern source has a very strong degree of polarization, which reaches up to 80% at the beginning of the rise phase and remains strong afterwards, ∼60%. In contrast, the degree of polarization of the stronger, Southern source is much weaker, being about 20% on average, but is strongly reduced during the impulsive phase when the 34 GHz emission has the strongest intensity. The spatially resolved microwave light curves display a prominent time delay between the southern and the northern sources, which implies that electron acceleration takes place at or close to the southern source, while the electrons reach the remote northern source only after traveling roughly 2 s through a coronal loop.

The first 2D image at 5.7 GHz is available at 01:37:11 UT, i.e., already in the decay phase. There is one single source which is displaced compared to any of the high-frequency sources in a manner implying loop-like connectivity between the NoRH sources; its centroid is located closer to the southern than to the northern NoRH source. The 5.7 GHz source evolves noticeably during the flare. Given that SSRT produces only one 2D map per 2–3 minutes, we employ 1D SSRT scans to study this evolution. The intersections of the dotted, dashed, and solid blue lines in Figure 7(a) (from right to left) show the locations

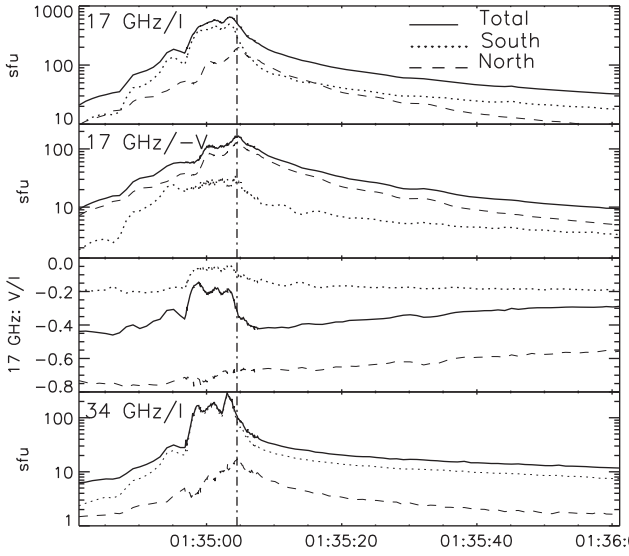

Figure 8. NoRH light curves: (a) flux densities from the northern and southern sources along with the integrated data at 17 GHz; (b) the same for the Stokes *V* parameters; (c) the same for degree of polarization; and (d) the flux densities at 34 GHz.

of the 5.7 GHz source centroid before, during, and after the impulsive phase of the event, respectively. Apparently, the source centroid moves eastward with a velocity estimated as 3.2×10^7 cm s^{-1} during the rise, peak, and early decay phases, and then stops moving such that its position is almost precisely the location of the 2D image taken at 01:37:11 UT. The apparent source sizes remain roughly constant during the burst,

being about $50'' \times 100''$, which implies the true sizes to be about $40'' \times 90''$ or less.

2.5. Summary of the Data

There are two striking features in the flare under study. The first feature is a prominent variation of the time profile impulsiveness, that is, from highly impulsive HXR and high-frequency microwave light curves (particularly, at 35 GHz) to increasingly gradual microwave light curves at progressively lower frequencies and SXR light curves. This makes it difficult to think of this event in terms of the conventional Neupert effect. Indeed, Figures 2(d) and (e) show that the light curves at 35 GHz or, equivalently, the HXR ones, do not correlate with the SXR time derivative, but correlate tightly with the derivative of the microwave light curve at 3.75 GHz. This correlation could imply that the 3.75 GHz light curve represents the thermal response of the heated plasma. However, the SXR time derivative correlates well with the 3.75 GHz light curve itself, which would instead imply that the 3.75 GHz light curve is most representative of the nonthermal particle impact. Thus, the classification of the light curves as thermal and nonthermal based solely on their impulsiveness becomes inconclusive in our event, which necesitates a more detailed analysis of the observed relationships.

The second striking property, which is closely related to the first, is the remarkable spectral evolution of the microwave burst. During the rise phase and the impulsive peak, the microwave spectrum displays a conventional (inverted bell-shaped) form with the spectral peak frequency well correlated with the peak flux (see Nita et al. 2004). This correlation is indicative of the optical thickness effect in the spectral peak formation (Dulk 1985; Melnikov et al. 2008). Then, at a later, gradual phase, the spectrum becomes essentially flat between 1 and 10 GHz. Overall, the spectral evolution can be characterized as a progressive low-frequency flattening over the course of the flare. This flattening can be understood if the microwave source is becoming more and more nonuniform with time. However, this is only a part of the puzzle; over the gradual phase, the degree of polarization is unexpectedly large at 3.75–5.7 GHz as well as at 17–35 GHz, which is indicative of optically thin emission at these spectral ranges and small at 1–2 GHz and 9.4 GHz, as expected for the optically thick emission. This implies that two distinct, nonuniform sources (presumably loops) are involved.

3. MODELING

The first of the two loops implied by the data, no doubt, produces nonthermal emission that dominates the impulsive component at high frequencies. The second loop produces gradual emission, which can be either thermal or nonthermal, that dominates at lower frequencies. We carefully address the question of whether this gradual emission is thermal or nonthermal and reject the thermal model; see the Appendix.

3.1. Nonthermal Model for the Gradual Flare Component

Given that we rejected the thermal model of the gradual emission component in the given flare, we turn now to a nonthermal model. The biggest challenge for a nonthermal model is to explain why the lower-frequency light curves have a longer decay constant than the higher-frequency ones; a property which holds all the way from 35 GHz down to 0.6 GHz. Indeed, the extended microwave emission is commonly ascribed to the fast electron fraction trapped in the coronal part of the flaring loop (often, the looptop) due to the magnetic mirroring effect (e.g., Melnikov 1994; Bastian et al. 1998; Melnikov & Magun 1998; Lee & Gary 2000; Lee et al. 2000; Kundu et al. 2001; Melnikov et al. 2002, and many others). Then, the fast electrons lose their energy due to Coulomb collisions. They are also scattered into the loss-cone and escape from the loop due to Coulomb scattering. The characteristic time constants of the energy loss and angular scattering due to Coulomb collisions both increase with electron energy; thus, the high-energy electrons survive longer in the coronal trap than do the lower-energy electrons. The higher-energy electrons radiate at higher frequency; thus, the higher-frequency microwave emission is supposed to have a longer decay time than the lower-frequency emission. This behavior has been observed in many cases, but our event displays the exact opposite trend.

To understand the likely causes of this unusual trend, we refer to a seminal paper by Lee et al. (1994), who thoroughly studied four X-class flares with unusually flat microwave spectra in the 1–20 GHz range; the X9.4 1991 March 22 flare from their sample demonstrates the closest resemblance to our event in terms of light-curve duration versus frequency. Lee et al. (1994) undertook a simplified 3D modeling with a dipole magnetic loop to interpret the observed properties of the microwave emission in their event sample. They found that for a dipole loop which is big and nonuniform (has a reasonably high mirror ratio), the microwave spectrum can be remarkably flat in a rather broad spectral range, even from 1 to 20 GHz for a sufficiently large magnetic loop. This conclusion is confirmed by more sophisticated 3D modeling reported by Kuznetsov et al. (2011).

In addition to the interpretation of the flat spectra at the flare peak phase, Lee et al. (1994) also offered an elegant and convincing scenario for the flare evolution, which naturally results in the observed "anomalous" behavior of the microwave light curves versus frequency. Originally, during the impulsive rise phase, the microwave source is relatively compact and occupies a volume with a relatively strong magnetic field, which results in high spectral peak frequency, $f_{\rm peak} \gtrsim 20$ GHz. Then, the radio source expands to occupy a much bigger nonuniform loop[10], and produces the flattest spectrum at that phase when the source becomes the most nonuniform (i.e., magnetic field varies over the broadest range of values). Later, during the decay phase, the radio source "shrinks" toward the looptop where the magnetic field is low, thus resulting in a decrease of the spectral peak frequency toward 1 GHz in the decay phase. Lee et al. (1994) noted that the fast electron spectral softening (with the electron spectral index δ change from around 3 at the peak phase to 4 at the decay phase) can further improve the consistency of the model microwave spectral evolution with the observed one. It is highly likely that a very similar scenario happened in our event, despite the fact that it is only a C5.1 *GOES* class flare, i.e., it is two orders of

[10] Lee et al. (1994) proposed an "inflated" magnetic loop, but a similar effect can be achieved if the fast electrons gradually fill an increasingly larger fraction of a large magnetic trap.

magnitude smaller than the X-class flares analyzed by Lee et al. (1994).

3.2. The Flare Morphology Suggested by the Data

The locations of and relationships between various EUV and microwave sources suggest that this flare belongs to the Hanaoka morphological type (Hanaoka 1997) where the flare energy release is believed to be driven by the interaction between a small compact loop whose footpoints are highlighted by the EUV kernels, and a bigger loop whose footpoints are highlighted by the high-frequency microwave sources at 17 and 34 GHz, while the coronal part of the loop is implied by the 5.7 GHz image. Remarkably, this two-loop configuration is supported by other available data. For example, there are neutral lines both between the EUV kernels and between the microwave footpoints, which indicates that the corresponding magnetic connectivities are likely.

Independent evidence in favor of two distinct sources comes from the microwave polarization spectrum. Indeed, the degree of polarization is very small at 1–2 GHz, indicating optically thick emission at these frequencies, but turns high at 3.75–5.7 GHz, manifesting optically thin emission. However, the degree of polarization is low again at 9.4 GHz, while once again high at 17–35 GHz. This behavior of the degree of polarization is entirely inconsistent with a single (though spatially nonuniform) source (Kuznetsov et al. 2011), but instead requires two distinct radio sources with strongly differing magnetic fields.

It is reasonable to assume that a smaller loop has a larger magnetic field while a larger loop has a weaker magnetic field, and therefore can form an efficient magnetic trap. The microwave light curves support this idea. Indeed, the high-frequency light curve at 35 GHz, which is supposed to originate from the source with the strongest magnetic field, is highly impulsive (as well as all HXR light curves) and does not show any evidence of fast electron trapping in a coronal loop. Thus, it is likely formed in the small loop with strong magnetic field and small mirror ratio, which makes the magnetic trapping inefficient. In contrast, the lower-frequency, optically thin light curve at 3.75 GHz has a delayed tail, as if the fast electrons were injected from the small loop (or from an interaction region of these two loops) and then accumulated into the bigger loop. This causal relationship is further supported by close correlation between the time derivative of the gradual 3.75 GHz light curve and the impulsive 35 GHz and HXR light curves.

3.3. Validating the Model with 3D Modeling

Even though the outlined flare model seems plausible, the current state-of-the-art requires that it be quantitatively validated by 3D modeling based on appropriate magnetic extrapolation, as in Fleishman et al. (2011, 2013, 2016), Nita et al. (2015), and Kuznetsov & Kontar (2015). However, the modeling is substantially complicated in our case for the following reasons. Since two different loops with presumably different twists are involved in the flaring process, it is unlikely that they could be reproduced within either the potential or linear force-free field (LFFF) extrapolation used in the cited studies addressing a single loop only, and so a nonlinear force-free field (NLFFF) extrapolation is called for. However, there is no vector magnetogram available to perform NLFFF extrapolation. We do have the line-of-sight magnetic data from SoHO/MDI, which is formally sufficient to produce an LFFF extrapolation, but it will necessarily be imperfect since the region of interest is located very close to the limb.[11] This implies that we can only perform a number of tests with the available data, but not a comprehensive modeling. In particular, we are forced to create two separate LFFF models with presumably different force-free parameters α—one for each of the two loops involved in our flare.

With this reservation, we employ the powerful GX Simulator tool (Nita et al. 2015) to test if there is a model (a set of two different data cubes—one for each loop) that is consistent with the photospheric magnetogram which can answer the following key questions about the event.

1. Can the implied small and big loops be reproduced in LFFF extrapolated data cubes and what α is needed for that?
2. Is it possible to populate the small loop with a distribution of fast electrons, which is consistent with the HXR data and, at the same time, capable of reproducing the high-frequency microwave spectrum?
3. Is it possible to populate the big loop with a distribution of fast electrons consistent with the HXR data to reproduce the low-frequency microwave spectrum?
4. Could the entire spectrum be reproduced by the two-loop model?
5. Is it possible to obtain the LCP polarization from both 17 GHz sources?
6. Is it possible to obtain a very high degree of LCP polarization from the north 17 GHz source?
7. Could the entire polarization spectrum be reproduced by the two-loop model?

Let us start with the model needed to reproduce the small loop. After some trial and error (see Fleishman et al. 2016) with the built-in LFFF engine of the GX Simulator (Nita et al. 2015), we obtained a narrow range of $\alpha \approx -1.75 \times 10^{-9}\,\mathrm{cm}^{-1}$ for which the connectivity between the EUV kernels can be reproduced as shown in Figure 9. The central field line (shown in red) has a length of $L_{\rm small} \approx 8.84 \times 10^{8}$ cm, the magnetic field value at the looptop[12] is $B_{\rm small,lt} \approx 620$ G, and the mirror ratio is less than two.

For microwave spectral modeling, we select the peak time at 01:35:03.600 UT. One of the key ingredients for the modeling is the shape of the distribution function of the nonthermal electrons. Although the microwave data themselves can be successfully fit by a single power-law distribution of fast electrons over energy,[13] we adopt here a broken power law as suggested by the KW X-ray fit (see Table 1). We obtain a reasonably good *spectral* match at high microwave frequencies if we populate this magnetic loop with a fast electron distribution (see Table 1, intervals 5–6) with $E_{\rm min} = 10$ keV, $E_{\rm br} = 150$ keV, $E_{\rm max} = 1.8$ MeV, $\delta_{\rm r,1} = 2.5$, $\delta_{\rm r,2} = 3.5$, and $N_{\rm r,}$

[11] Typically, a model built from an LFFF extrapolation close to the limb requires that the model magnetic field be scaled by a small number.

[12] A scaling factor of three was applied to the originally extrapolated magnetic data cube (see Fleishman et al. 2016).

[13] This is because the microwave spectrum at these high frequencies is not sensitive to the exact shape of the nonthermal electron spectrum at low energies where the break of this spectrum is suggested by the KW data. This results in a well-known uncertainty while estimating the energy content and other measurements determined by the low-energy part of the nonthermal electron spectrum.

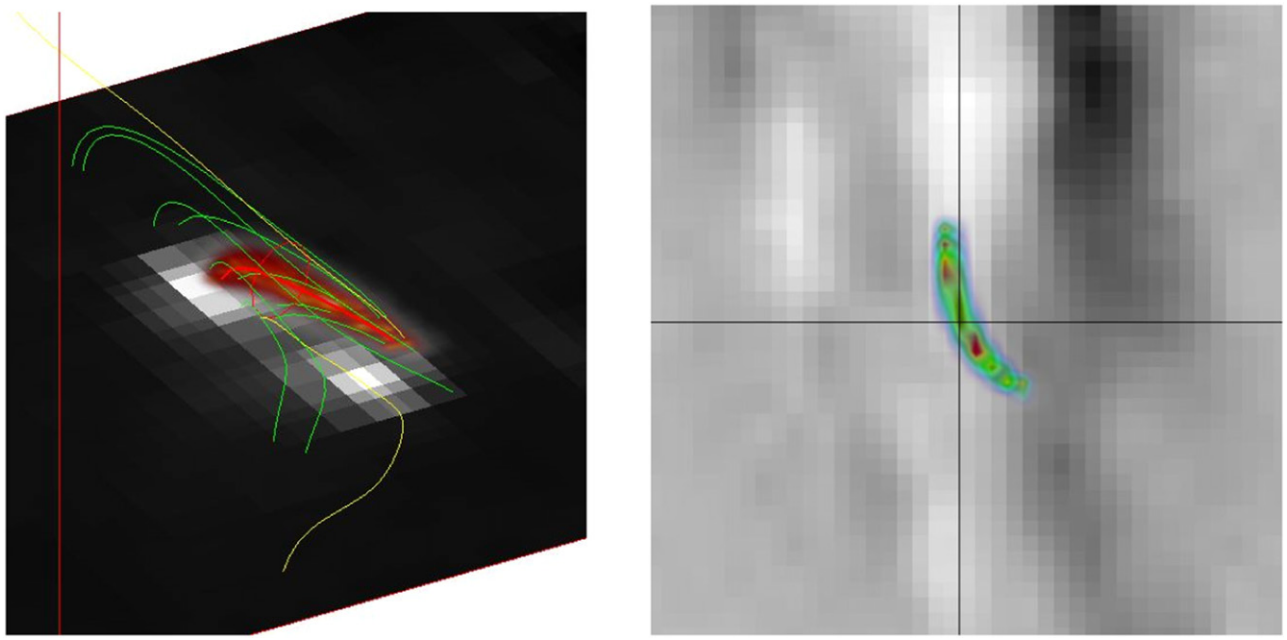

Figure 9. Small loop connecting two 195 Å kernels built out of the LFFF extrapolation with $\alpha \approx -1.75 \times 10^{-9}$ cm^{-1}. Left: perspective view with the EUV difference background image, magnetic structure visualized with a few closed (green) and open (yellow) field lines, central field line of the flaring flux tube (red), and thermal electron density distribution (diffuse dark red volume). Right: number density of the fast electrons (diffuse green volume) on top of the LOS MDI magnetogram (top view).

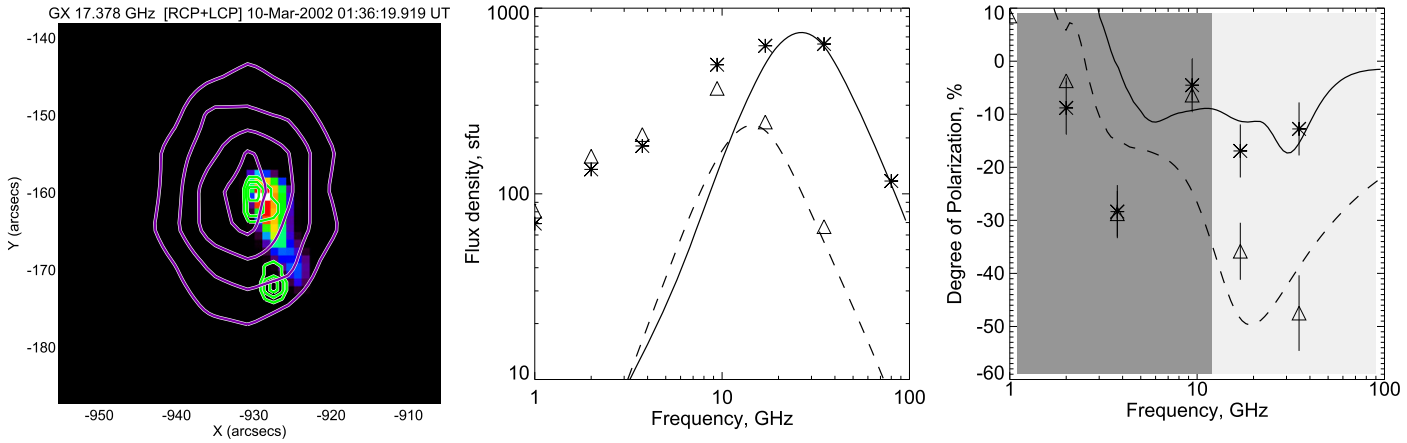

Figure 10. Key outcome of the small loop modeling of high-frequency emission (above 10 GHz). Left: synthetic microwave image at 17 GHz computed from the adopted model along with EUV 195 Å difference image (green contours) and NoRH 17 GHz image of the southern source (violet contours). Middle: observed total power spectrum at the microwave peak time (01:35:03.600 UT, asterisks) and early decay phase (01:35:08 UT, triangles) and the corresponding model spectra from beam-like (solid line) and isotropic (dashed line) angular distributions. Right: observed degree of polarization at the same times and corresponding polarization spectra for beam-like (solid line) and isotropic (dashed line) angular distributions. Only the area on top of the light gray background is relevant for the model-to-data comparison.

$_{\rm tot} \sim 10^{34}$ electrons distributed roughly uniformly over the loop length and isotropically over the pitch-angle. The thermal number density has almost no effect on this high-frequency emission: we varied the number density from 10^{10} to 5×10^{11} cm^{-3} with essentially no modification of the spectrum. The *sense* of polarization corresponds to the LCP wave at high frequencies in agreement with observations, but the *degree* of polarization is much stronger than observed. The degree of polarization can be reduced by either a tangled magnetic field structure at the source or a beam-like anisotropy of the accelerated electrons (Fleishman & Melnikov 2003). We investigated the possible effect of the beam-like anisotropy in our case and found that it offers a much better match (solid curves in Figure 10) to the measured degree of polarization at the impulsive peak than the isotropic distribution (dashed curves in Figure 10). The best fit is obtained for the number density of the fast electrons $n_{\rm r} = 5.2 \times 10^8$ cm^{-3} (this is the peak value of the spatially nonuniform electron distribution) that corresponds to the total number of fast electrons at the source $N_{\rm r,tot} \approx 1.35 \times 10^{34}$. Note that the electron acceleration rate determined from the X-ray fit is about 1.2×10^{35} electron s^{-1}, which implies that the electron escape time $\tau_{\rm esc}$ from the loop is roughly 0.1 s, which is three times larger than the time of flight ($L_{\rm small}/c \sim 30$ ms) estimated for our loop length $L_{\rm small} \sim 9 \times 10^8$ cm. Given that the electron distribution is found to be beamed along the field lines, while the mirror ratio in this loop is small, ~2, a more reasonable estimate for the escape time would be within 30 ms; this upper

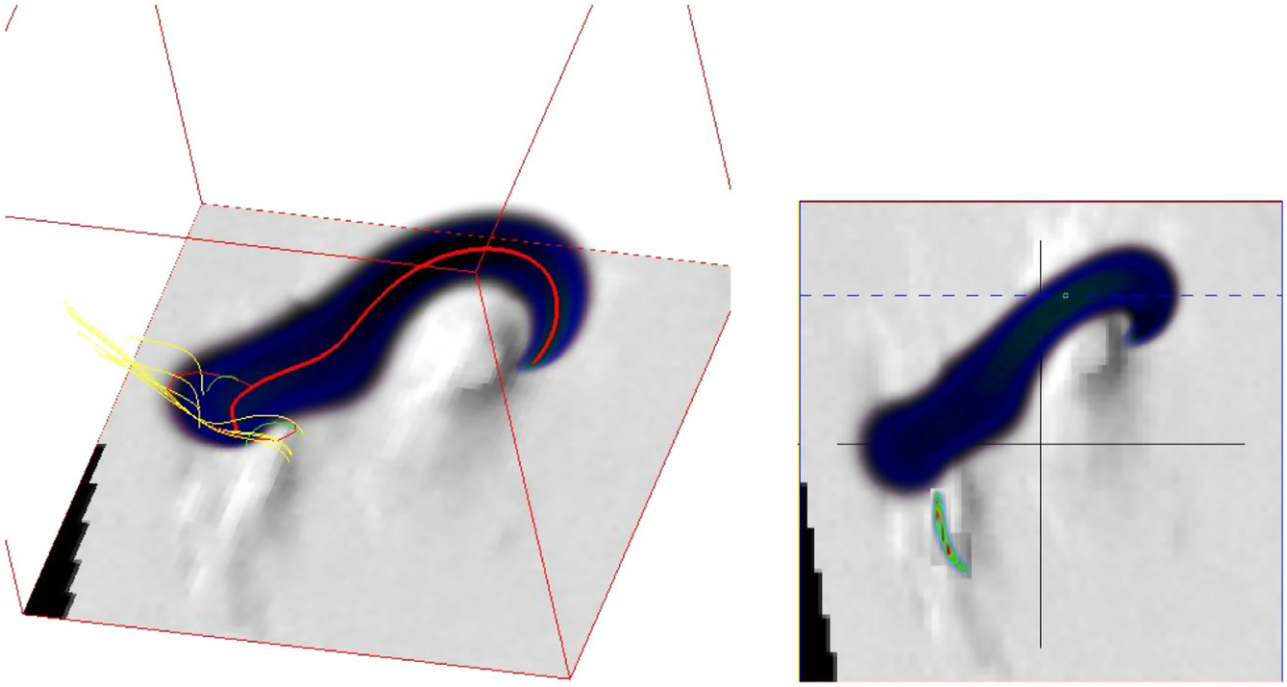

Figure 11. Big loop connecting two NoRH 17 GHz sources (northern and southern) built out of the LFFF extrapolation with $\alpha \approx 1.16 \times 10^{-9}$ cm^{-1}. Left: perspective view with the MDI LOS magnetogram background image, cental field line of the flaring flux tube is shown in red, and the nonthermal electron density distribution shown in diffuse dark volume. Right: top view with the small loop (green volume) added in scale.

limit for the escape time is also implied by the absence of any measurable (within 0.1 s time resolution) delay between the 35 GHz light curve and the HXR light curves. Our two-loop model offers a natural solution for this discrepancy: with the numbers above, we conclude that, in fact, the acceleration rate is roughly two times larger than that derived from the HXR fit, but the remaining (~50%) accelerated electrons escape to the second, big loop,[14] rather than precipitating to the small loop footpoints; thus, they do not contribute to the HXR emission.

Apparently, we can estimate the escape time from the 35 GHz light curve decay time τ, which is roughly 1 s, in even stronger contradiction with the 0.03 s determined above. A reasonable way to reconcile this contradiction is to ascribe the decay segment of the light curve to the residual electron component trapped in the small loop. If such is the case, then this residual component must be substantially more isotropic than the original beamed distribution at the impulsive acceleration phase. The implied evolution of the pitch-angle distribution from a beamed to a more isotropic or loss-cone distribution must leave a fingerprint in the corresponding evolution of the degree of polarization. Indeed, as we noted in Section 2.2 (see Figure 2(f)), the degree of polarization goes up at 17 and 35 GHz during the early decay phase. It is interesting that the polarization data at this decay phase are quantitatively consistent with the isotropic distribution of the radiating electrons. Indeed, the model degree of polarization (dashed curve) agrees well with the data shown with the triangles in Figure 10, right. The model assumes the number density of the fast electrons to be $n_r = 6 \times 10^7$ cm^{-3}, which corresponds to the total number of fast electrons at the source $N_{r,tot} \approx 8 \times 10^{32}$ and the same spectral parameters as at the peak phase. The corresponding observed (triangles) and model (dashed curve) flux densities are shown in the middle panel of Figure 10.

Let us turn to the big loop modeling. We use now a bigger field of view covering both the northern and southern microwave sources. Building a big loop in the right place is possible for extrapolated data cubes with positive α centered around the value $\alpha \approx 1.16 \times 10^{-9}$ cm^{-1}. The center field line of the model loop has a length of $L_{big} \approx 8.2 \times 10^9$ cm, the magnetic field value at the looptop[15] $B_{big,lt} \approx 30$ G, and a mirror ratio of about four, see Figure 11. We note that the nonthermal electron distribution in the big loop is more poorly constrained than that in the small loop because the accelerated electron distribution, before arriving at the big loop, is modified by the energy-dependent escape time from the small loop/acceleration region, and then by the energy-dependent trapping time in the big loop. Moreover, we have only limited information about the high-frequency slope of the microwave emission from the big loop from the spatially resolved NoRH data, while the TP NoRP data are dominated by the small loop as explained above. Given all these uncertainties, for the big loop we adopt a single power-law energy spectrum of the nonthermal electrons with the same (high-energy) spectral index as for the small loop, $\delta_r = 3.5$.

For spectral modeling of the big loop contribution, we select the time 01:35:24.500 UT at the decay phase—rather close to the end of the prominent spectral evolution where emission from the big loop presumably dominates the microwave spectrum. We obtain a reasonably good spectral match at low frequencies if we populate this magnetic loop with a fast electron distribution within the energy range starting from the same $E_{min} = 10$ keV in agreement with both HXR data and the

[14] A fraction of the nonthermal electrons can also escape along the open field lines.

[15] A scaling factor of 0.58 has been applied to the originally extrapolated magnetic data cube.

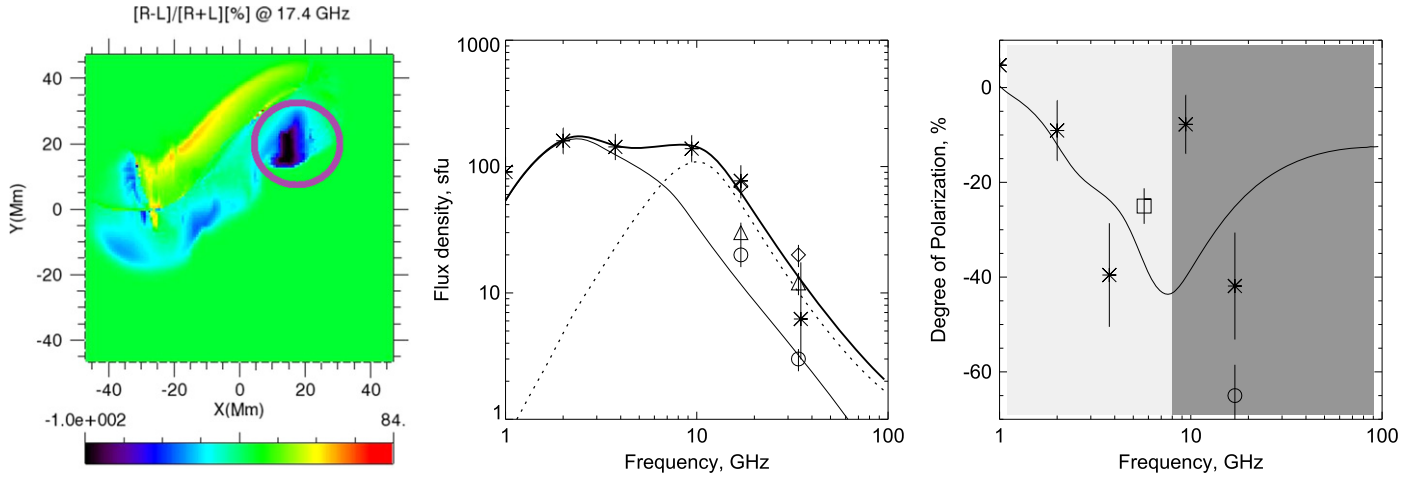

Figure 12. Key outcome of the big loop modeling. Left: synthetic microwave polarization image at 17 GHz computed from the adopted model along with NoRH 17 GHz highly polarized Northern source (violet contour). Middle: observed total power spectrum at the decay phase (01:35:24.500 UT; asterisks) and spatially resolved NoRH data at 17 and 34 GHz from the northern source (open circles), the southern source (triangles), and total (diamonds) along with the corresponding model spectra from the big loop (thin solid line), the small loop (dotted line), and sum of them (thick solid line). Right: observed degree of polarization at the decay phase (01:35:24.500 UT) from NoRP (triangles), SSRT at 5.7 GHz (square), and northern NoRH source at 17 GHz (open circle) and the corresponding synthetic polarization spectrum produced by the big loop (solid line). Only the area on top of the light gray background is relevant for the model-to-data comparison.

small loop model to $E_{\max} = 5$ MeV,[16] and the number density $n_r = 1.6 \times 10^7$ cm^{-3} totaling in $N_{r,tot} \approx 5.7 \times 10^{34}$ electrons slightly concentrating toward the looptop, as expected due to particle trapping effect in the magnetic loops (Melnikov et al. 2002). The angular distribution is expected to have a loss-cone shape with a loss-cone angle of $\theta_{lt} = 30°$ in the top of the loop, which is in agreement with a mirror ratio of four. In fact, the isotropic distribution was found to give the same results, and so here we give the numbers relevant to the isotropic model, which is computationally faster than the anisotropic one. The thermal plasma density at the central field line of the big loop is adopted to be $n_0 = 5 \times 10^9$ cm^{-3}. This model offers a very good match for the low-frequency part of the TP spectrum and also reproduces the correct level of spatially resolved data from the northern NoRH source at 17 and 34 GHz, although the flux density of the northern source at 17 GHz is slightly underestimated. Similarly, the model slightly underestimates the flux density at 1 GHz, which indicates that the real source has a slightly stronger nonuniformity than the model one (see the 3D models in Kuznetsov et al. 2011).

The model reproduces trends for the degree of polarization. Indeed, as is seen from the right panel of Figure 12, the degree of polarization is close to zero at 1 GHz, while it is negative and relatively strong at 2 and 3.75 GHz—all in agreement with observations. However, values of the model degree of polarization at 1 and 3.75 GHz deviate from the observed values by a factor of two. We varied the angular distribution of the fast electrons in the big loop, but this did not remove the mismatch of the polarizations. We conclude that the mismatch is likely due to the imperfect geometry of the model loop compared to the real source (recall, the degree of polarization is highly sensitive to the viewing angle), which is very possible given the limitations of our modeling due to the lack of constraints discussed in the beginning of this section.

Finally, we checked and confirmed that the combination of these two loops is capable of matching the entire microwave spectrum at a given time; to illustrate that we selected the same time frame 01:35:24.500 UT, see the thick solid line in Figure 12. Although the solution is far from unique, we can obtain a very good match to the entire spectrum between 1 and 35 GHz by adding emission (dotted line in Figure 12) from a small loop with the same central field line as in the impulsive phase, but having a somewhat broader spatial distribution of the accelerated electrons transversely to this central field line. A consistent fast electron distribution has a number density for the fast electrons $n_r = 1.5 \times 10^6$ cm^{-3} that corresponds to the total number of fast electrons at the small loop $N_{r,tot} \approx 1.1 \times 10^{32}$ distributed isotropically with a modest concentration at the looptop (see Melnikov et al. 2002), and with the same broken power-law spectral shape. Given that we did not obtain a quantitative match for the degree of polarization at low frequencies, we did not try to match the entire polarization spectrum with the two-loop model.

With the described modeling we got a definitive "yes" for questions 1–6 raised in the beginning of this section. The answer to the seventh question is quantitatively less definitive: we failed to quantitatively reproduce the degree of polarization at many of the frequencies or time frames analyzed. Nevertheless, we did obtain a generally correct trend in all of the cases. Indeed, the sign of the degree of polarization is reproduced correctly for all of the time frames and at all of the frequencies; the model numbers are consistent with the observed ones within a factor of two. When we obtained a larger mismatch, we found a much better match by adjusting the pitch-angle distribution of the fast electrons, which gave us additional important constraints on the model. We conclude that the proposed flare model based on two interacting loops is fully validated by the modeling performed here.

4. DISCUSSION

We have described a puzzling cold flare event observed in the X-ray domain with *GOES* and KW and in the microwave domain by a number of instruments in a rather broad spectral range, covering more than two orders of magnitude in frequency—from 0.6 to 80 GHz. This flare displays a number

[16] Although the value of $E_{\max}$ is poorly constrained by the data, smaller $E_{\max}$ would result in a progressively stronger underestimation of the flux density at 34 GHz (open circle) from the northern source; Figure 12, middle.

of truly exceptional properties in all of these domains. The HXR emission extends well above 1 MeV and displays one of the hardest energy spectra ever detected (Vestrand et al. 1999) for a C-class flare. In SXR, the *GOES* light curves are substantially delayed compared to what is expected according to the Neupert effect. In microwaves, there are a number of peculiarities. The spectral peak frequency displays an exceptional variation over the burst between at least 35 GHz at the impulsive peak down to 1.5 GHz at the decay phase—the property observed for some of the strongest events, but clearly at odds for a modest C-class flare. The microwave light curves show a remarkable diversity of shapes—from very impulsive and highly correlated with HXR light curves at 35 GHz, to increasingly gradual at lower and lower frequencies—again, observed for a few X-class flares, but not for modest events. However, this exceptional spectral evolution takes place only over the impulsive phase and early decay phase, but then the spectral evolution switches off at some point and the microwave emission slowly decays with a constant spectral shape. In addition, during this remarkable spectral evolution stage, the coronal part of the microwave source moves rapidly eastward with a velocity of $320\,\mathrm{km\,s^{-1}}$, but then stops and stays at the same location during the remaining decay phase.

The data analysis and 3D modeling suggest that all of the remarkable properties of this event can quantitatively be understood within a model involving energy release due to the interaction of two non-potential magnetic flux tubes—one small and one big with different twists ($\alpha \approx -1.75\times10^{-9}\,\mathrm{cm^{-1}}$ and $\alpha \approx 1.16\times10^{-9}\,\mathrm{cm^{-1}}$, respectively). Electrons are accelerated due to the interaction (magnetic reconnection) between these two loops and then divided in roughly equal numbers between these two loops. The electrons injected into the small loop have a beam-like distribution directed toward the southern EUV kernel. This finding concerning the beamed pitch-angle distribution of the nonthermal electrons is highly important for understanding the electron acceleration and transport, yet no routine diagnostics of the electron angular distribution is available. Kontar & Brown (2006) and Dickson & Kontar (2013) used the effect of the photospheric albedo on the HXR spectrum to conclude that nonthermal electron distribution is close to isotropic, while inconsistent with a noticeable beaming. However, this conclusion pertains to the chromospheric target volume, rather than to the coronal source. Fleishman (2006) employed microwave polarimetry to reveal the loss-cone anisotropy of the trapped component of the nonthermal electrons, while Altyntsev et al. (2008, 2016) and Melnikov et al. (2014) reported beam-like anisotropy for some events. It is interesting that Altyntsev et al. (2008, 2016) found beam-like anisotropy in smaller loops in two events involving interaction between two different loops, which is in line with the finding discussed here.

Due to the beamed angular distribution, most of the streaming nonthermal electrons immediately precipitate into the southern footpoint of the small loop and produce HXR emission there. On the fly, they interact with the magnetic field of the loop, which is reasonably strong in the small loop, varying from $B\sim600$ G at the looptop up to $B\sim1200$ G at the footpoints, to produce the high-frequency microwave emission as observed. The total number of fast electrons, $N_{\mathrm{r,tot}}\approx 1.35\times10^{34}$, needed to match the high-frequency part of the microwave spectrum at the peak time requires an acceleration rate nearly double that derived from the HXR thick-target model fit, $\sim1.2\times10^{35}\,\mathrm{electron\,s^{-1}}$.

The missing electrons, those not seen via HXR emission, must have escaped to the big loop and been trapped there. To confirm this quantitatively, we note that at the decay phase time frame, 01:35:24.500 UT, which we analyzed in great detail to validate the model, the total number of trapped fast electrons was found to be $N_{\mathrm{r,tot}}\approx 5.7\times10^{34}$ to match the microwave spectrum. This implies that at the peak time of the gradual microwave light curves (01:35:05 UT), when the flux density at 3.75 GHz is twice as large as at 01:35:24.500 UT, the number of nonthermal electrons in the big loop must have been a factor of two larger, $N_{\mathrm{r,tot}}\approx 1.2\times10^{35}$. This peak number of the fast electrons accumulated in the big loop is to be compared with the corresponding electron injection into the big loop. If we assume that the electron injection rate into the big loop is equivalent to the electron loss rate derived from the HXR thick-target spectral fit, then the total number of electrons injected into the big loop would be $N_{\mathrm{inj}}\sim 6\times10^{35}$ electrons over the impulsive phase of the flare; which, taken at face value, is roughly five times larger than is needed to supply the observed microwave emission from the big loop. Given that the number of nonthermal electrons in the big loop is determined using a poorly defined low-energy spectral index and low-energy cutoff in the big loop, we conclude that the obtained electron numbers are consistent with each other. Escape of half of the accelerated electrons, or slightly less, toward the big loop is sufficient to supply it with the required number of fast electrons needed to match the low-frequency part of the microwave spectrum.

This picture is also quantitatively consistent with the light curves for various frequencies and energies. Indeed, the close correlation between the HXR (or 35 GHz) light curves and the time derivative of the 3.75 GHz light curve is consistent with the former being a proxy of the acceleration/injection time profile, while the latter is a proxy of the trapped electron component. Now, the delay in the SXR *GOES* light curves becomes transparent: the direct losses of the accelerated electrons immediately available for plasma thermal response (including heating and evaporation) are limited to only roughly half of all electrons, which precipitate through the small loop. The other half of accelerated electrons trapped in the big loop lives longer and continues to heat the plasma via in situ Coulomb collisions in the loop and precipitation. This is why the *GOES* flux and the *GOES*-derived temperature continue to grow well after the impulsive phase of the flare is over. We emphasize that such a scenario is only possible if the accelerated electrons are roughly equally divided between these two loops, as is the case in our model, which additionally confirms the fast electron numbers obtained above for these two loops from the independent microwave spectrum fits.

Having validated the model, we can now address a number of fundamental questions about magnetic reconnection, particle acceleration, and transport. Recall that the coronal microwave source moves quickly with an apparent velocity of roughly $320\,\mathrm{km\,s^{-1}}$ passing about 35″ over 80 s during the impulsive phase, which is reasonable to associate with a spread of the magnetic reconnection between the small and big loops. The process of magnetic reconnection will form new closed field lines (flux tubes) where the magnetic flux Φ is conserved along the field line (see, e.g., Qiu et al. 2009), such as $\Phi\sim V_{\mathrm{r}}B_{\mathrm{r}}\tau L_{\mathrm{r}}\sim V_{\mathrm{lt}}B_{\mathrm{lt}}\tau L_{\mathrm{lt}}$, where V_{r}, B_{r}, and L_{r} are the velocity, magnetic field,

and spatial scale at the reconnection site (site of interaction between the loops), $V_{\rm lt}$, $B_{\rm lt}$, and $L_{\rm lt}$ are the same at the looptop, and τ is the time of the reconnection process. Given that we know the magnetic field at the looptop from the modeling, $B_{\rm big,lt} \approx 30$ G, the looptop source velocity, and displacement, we can estimate the reconnecting electric field as $E_{\rm r}[{\rm V\,cm^{-1}}] \sim 10^{-3}\, B_{\rm lt}[{\rm G}] V_{\rm lt}[{\rm km\,s^{-1}}] \sim 10\ {\rm V\,cm^{-1}}$. Since the magnetic field at the small loop is more than two orders of magnitude larger than $B_{\rm lt} \approx 30$ G, the expected displacement of the reconnection site along the small loop is within $3''$ and unobservable, which is in agreement with the constant location of the southern microwave source. It is possible that this spatial extent of the reconnection is responsible for the increase of the small loop width required to get a good microwave fit at the decay phase.

This process of magnetic reconnection results, directly or indirectly, in the acceleration of a significant number of fast electrons to relativistic energies on a subsecond timescale. Interestingly, the microwave polarization data require that the accelerated electron distribution in the small loop be beamed along the magnetic field vector (i.e., from the northern source having the positive, north, magnetic polarity toward the southern source, having the negative, south, magnetic polarity). Recall that the small loop has a negative α, which implies that the electric field vector is directed oppositely to the magnetic field vector; thus, the fast electrons are beamed in the direction where they are driven by the electric field; thus, the electric field is a likely cause of this electron beaming toward the southern footpoint.

The thermal electron number density in the small loop is poorly constrained. but given that the fast electron number density is about $10^9\,{\rm cm^{-3}}$, the total electron number density is at least that big. On the contrary, we can obtain a good estimate of the thermal electron number density at the big loop using the microwave spectral shape at the late decay phase. Indeed, the spectral peak frequency remains constant late in the event, $\approx$1.5 GHz, while the low-frequency spectral index is rather large, $\alpha_{\rm lf} \approx 3$, which are collectively indicative of the spectral peak being formed by the Razin-effect $f_{\rm peak} \approx f_{\rm R}$, rather than the optical thickness effect, at the late decay phase. Given that the Razin frequency $f_{\rm R} \approx 20\ n_0/B$ and $B \approx 30$ G, we estimate the mean thermal number density at the big loop as $n_0 \sim$ (2–3) $\times\ 10^9\,{\rm cm^{-3}}$, which agrees well with the developed 3D model ($n_0 = 5 \times 10^9\,{\rm cm^{-3}}$ at the central field line of the loop and decreasing in the transverse direction over a Gaussian law).

Note that the collisional loss time in such a tenuous plasma is longer that one minute for all electrons with energies higher than 100 keV responsible for microwave emission, while the observed decay time of the light curve at 3.75 GHz, for example, is about $\tau \sim 30$ s. This unambiguously suggests that the high-energy, fast electron loss from the big loop is mediated by the process of enhanced electron pitch-angle scattering by turbulence and their escape from the loop via the loss-cone. This is independently confirmed by the lack of electron spectral flattening, which must be present in case of collisionally mediated electron transport.

In contrast, the low-energy electrons around the nominal low-energy cut-off of 10 keV are likely strongly affected by in situ Coulomb losses. Indeed, the collisional loss time for 10 keV electrons in a plasma with a number density around $2 \times 10^9\,{\rm cm^{-3}}$ is about 3 s. The corresponding energy deposition to the coronal plasma is roughly $\dot{E} = \int_{E_{\rm min}}^{E_{\rm max}} n_{\rm r}(E) E/t_E\, dE \approx 0.2\ {\rm erg\,cm^{-3}\,s^{-1}}$, where $n_{\rm r}(E)$ is the nonthermal electron distribution over energy and t_E is the collisional loss time (see Section 4 in Bastian et al. 2007). Accordingly, the temperature increase over the interval τ is $\Delta T \sim \frac{\tau \dot{E}}{3 n_0 k_{\rm B}}$, where $k_{\rm B}$ is the Boltzman constant; taking the observed duration of the main heating phase $\tau = 30$ s and plugging in other relevant numbers, we obtain $\Delta T \sim 7$ MK in agreement with *GOES* data. Thus, the energy-containing, low-energy electrons deposit their energy directly to the coronal plasma, while the less numerous precipitating, higher-energy electrons do not deposit sufficient energy to the footpoints to drive efficient chromospheric evaporation. This explains why we have a relatively strong microwave burst (which statistically corresponds to a M4-class event), but a rather weak C5 *GOES* flare. We conclude that we have obtained a fully consistent picture of this cold flare event.

5. CONCLUSIONS

In this study, we identified a new "cold" solar flare whose properties and physical model are substantially different from the cold flares reported so far (Bastian et al. 2007; Fleishman et al. 2011; Masuda et al. 2013). In contrast to the known cold flares, which consisted of one main loop, the flare described here from 2002 March 10 is a vivid example of the interaction between two loops. The first loop, a small one, is responsible for the impulsive flare component, while the bigger loop is responsible for more gradual nonthermal emission. Interestingly, the electrons accelerated in the event divided roughly evenly between these two loops, which made both loops comparably important in driving the thermal response in this event. For this reason, the *GOES* flare was substantially delayed relative to the impulsive peak, in apparent contradiction to the conventual Neupert effect. Deviations from the nominal Neupert effect have widely been reported (e.g., Veronig et al. 2002; Dennis et al. 2003; Veronig et al. 2005; Su et al. 2008) and often interpreted as evidence in favor of an additional source of plasma heating. However, no additional heating is needed to understand the heating delay in our event: taking into account the in situ coronal losses of the fast electron component trapped in the big loop, we obtained a scenario fully consistent with plasma heating by the accelerated electrons—which is in remarkable agreement with spirit of the Neupert effect. The developed model is in quantitative agreement with observations, including microwave imaging and polarization, and naturally identifies the cause of the suppressed chromospheric evaporation that is needed to interpret the unusually weak *GOES* response in this flare.

This work was supported in part by NSF grants AGS-1250374 and AGS-1262772, NASA grant NNX14AC87G to the New Jersey Institute of Technology, and RFBR grants 15-02-01089, 15-02-03717, 15-02-03835, 15-02-08028, and 16-02-00749. This study was supported by the Program of basic research of the RAS Presidium No. 9. The authors acknowledge the Marie Curie PIRSES-GA-2011-295272 RadioSun project. We thank Dr. Gelu Nita for encouraging discussions.

APPENDIX
THERMAL MODEL FOR THE GRADUAL FLARE COMPONENT

Let us consider a model in which the thermal emission plays a role at low frequencies, while the nonthermal

gyrosynchrotron emission dominates the high frequencies, although it can have some contribution at low frequencies. There are two main mechanisms of thermal emission in the microwave range—free–free and gyro emission (gyroresonance, GR, or gyrosynchrotron, GS). Note that the opacity of the free–free emission *decreases* as the plasma temperature *increases*. Thus, plasma heating alone results in a decrease of the microwave free–free emission while its increase requires a simultaneous significant increase of the plasma density to numbers inconsistent with the EM estimate available from the SXR *GOES* data; the peak value is EM $\approx 2 \times 10^{48}\,\mathrm{cm}^{-3}$. Therefore, if the observed emission is thermal, it can only be the gyro emission.

The weak polarization at 1 and 2 GHz tells us that the GR emission at these frequencies must be optically thick, while a significantly stronger polarization at 3.75 and 5.7 GHz implies that only the dominant X-mode (LCP in our case) may remain thick, while the O-mode (RCP) is becoming thin here. As long as the thermal emission remains optically thick, its flux in each of the eigen-modes (X and O) at a given frequency f is firmly specified by a product of the plasma temperature T and the source area A, such as

$$F_{\rm LCP} \simeq F_{\rm RCP} \simeq 6\ [\mathrm{sfu}]\left(\frac{f}{1\ \mathrm{GHz}}\right)^2\left(\frac{T}{10^7\ \mathrm{K}}\right)\left(\frac{A}{10^{20}\ \mathrm{cm}^2}\right), \quad (6)$$

and the total flux is equal to the sum of the two components, $F = F_{\rm LCP} + F_{\rm RCP}$.

Let us first consider the implications of the thermal model for the emission at 5.7 GHz where we have imaging data needed to estimate the source sizes and area. As has been estimated from Figure 7, left, the source sizes are $40'' \times 90''$, i.e., $A \simeq 2 \times 10^{19}\,\mathrm{cm}^2$, while $F_{\rm LCP} \simeq 100$ sfu; thus, Equation (6) yields the plasma temperature around $T \sim 25$ MK. This number looks somewhat excessive compared with the *GOES*-derived temperature (Figures 2(d) and (e)), however, it can still be fine if the plasma is tenuous and the corresponding EM is small. Let us estimate the thermal plasma number density from the light-curve cooling profile (the 5.7 GHz light curve, not shown in Figure 2, is similar to that at 3.75 GHz). It is easy to estimate that the radiative cooling time is much longer than the observed decay timescale $\tau_{5.7\ \mathrm{GHz}} \sim 30$ s; thus, the cooling must be controlled by the thermal conduction, whose timescale is (see Equation (4.3.10) in Aschwanden 2005)

$$\tau \simeq 2.4 \cdot 10^3\ [\mathrm{s}]\left(\frac{L}{10^{10}\ \mathrm{cm}}\right)^2\left(\frac{n_e}{10^{10}\ \mathrm{cm}^{-3}}\right) \times \left(\frac{10^7\ \mathrm{K}}{T}\right)^{5/2}, \quad (7)$$

provided that the heat conduction has not yet reached the free-streaming limit. Therefore, to obtain the right timescale of conductive cooling from the observed loop with length $L \sim 10^{10}$ cm and temperature $T \sim 25$ MK requires that $n_e \sim 10^9\,\mathrm{cm}^{-3}$; combined with the loop volume (assuming the sizes of $40'' \times 40'' \times 100''$ as observed), this density yields the emission measure EM $\sim 10^{46}\,\mathrm{cm}^{-3}$, which is more than two orders of magnitude smaller than the *GOES*-derived background value, and thus no *GOES* response is expected from this hot plasma. We conclude that the thermal model of the emission at 5.7 GHz does not contradict the available observational constraints.

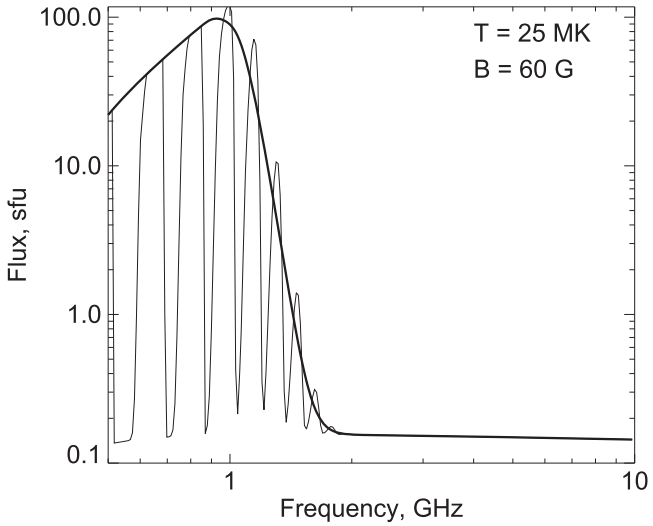

Figure 13. GS thermal spectrum plotted for a source with area $A = 4 \times 10^{20}\,\mathrm{cm}^2$, depth $d = 7 \times 10^8$ cm, $T = 25$ MK, thermal density $n_0 = 10^9\,\mathrm{cm}^{-3}$, $B = 60$ G, and viewing angle $\theta = 75°$. The thin curve shows the exact spectrum from a uniform source containing the gyroharmonics, while the thick curve shows the corresponding averaged spectrum obtained using the continuous fast code (Fleishman & Kuznetsov 2010). Smaller magnetic field will result in lower spectral peak frequency.

Having said that, we have yet to check whether or not this conclusion holds at lower frequencies. Now, we concentrate on the lower frequency of 1 GHz. The problem here is that the radio flux from a uniform thermal source scales as $\propto f^2$ with frequency (see Equation (6)) while we observe an almost flat spectrum, which implies that the product $A \cdot T$ must scale roughly as $\propto f^{-2}$. We do not have spatially resolved measurements at 1 GHz, so let us first consider the case of the same temperature $T \sim 25$ MK but bigger area $A \sim 4 \cdot 10^{20}\,\mathrm{cm}^2$ needed to provide the observed flux density at 1 GHz.

Given the implied increase of the source size at 1 GHz compared with that at 5.7 GHz, the conductive cooling time is consistent with the observed value $\tau_{1\ \mathrm{GHz}} \sim 150$ s for roughly the same number density $n_e \sim 10^9\,\mathrm{cm}^{-3}$. However, the enhanced source area also implies an enhanced volume, $V \sim 3 \cdot 10^{30}\,\mathrm{cm}^3$, which yields an emission measure of EM $\sim 3 \cdot 10^{48}\,\mathrm{cm}^{-3}$. Such an EM would easily be revealed by *GOES* data on top of a comparable background value, which is not observed, and thus calls the thermal model into question. On top of that, to obtain optically thick thermal GR emission with a brightness temperature of 25 MK from a given line of sight at 1 GHz, the line of sight must cross a volume element with $T \sim 25$ MK and the magnetic field must equal or exceed 60 G (see Figure 13). Figure 7, right, shows the projected area of all lines of sight satisfying the condition $|B| > 50$ G from the magnetogram directly, from which we can directly compute the maximum possible area of such a thermal gyro source as $A\ (>50\ \mathrm{G}) \approx 4.77 \cdot 10^{19}\,\mathrm{cm}^2$, which is insufficient by almost one order of magnitude to reproduce the observed radio flux at 1 GHz. Our tests with 3D modeling using the extrapolated magnetic data cube confirm that even if we fill the entire data cube with hot plasma having $T \sim 25$ MK, the mismatch between the modeled and observed flux at 1 GHz is more than a factor of two, regardless of the selected combination of input

parameters. Having a higher temperature would imply an accordingly bigger density to keep the conductive cooling time the same as observed. However, this enhanced density yields an enhanced EM in progressive disagreement with the *GOES* data. We conclude that the thermal model is not supported by the data.

REFERENCES

Altyntsev, A. T., Lesovoi, S. V., Meshalkina, N. S., Sych, R. A., & Yan, Y. 2001, A&A, 400, 337
Altyntsev, A. A., Meshalkina, N. S., Fleishman, G. D., Myshyakov, I., & Pal'shin, V. 2016, SoPh, submitted
Altyntsev, A. T., Fleishman, G. D., Huang, G.-L., & Melnikov, V. F. 2008, ApJ, 677, 1367
Aptekar, R. L., Frederiks, D. D., Golenetskii, S. V., et al. 1995, SSRv, 71, 265
Arnaud, K. A. 1996, in ASP Conf. Ser. 101, Astronomical Data Analysis Software and Systems V, ed. G. H. Jacoby, & J. Barnes (San Francisco, CA: ASP), 17
Aschwanden, M. J. 2005, Physics of the Solar Corona. An Introduction with Problems and Solutions (2nd ed.; chichester: Praxis Publishing)
Bastian, T. S., Benz, A. O., & Gary, D. E. 1998, ARA&A, 36, 131
Bastian, T. S., Fleishman, G. D., & Gary, D. E. 2007, ApJ, 666, 1256
Brown, J. C. 1971, SoPh, 18, 489
Dennis, B. R. 1988, SoPh, 118, 49
Dennis, B. R., Veronig, A., Schwartz, R. A., et al. 2003, AdSpR, 32, 2459
Dickson, E. C. M., & Kontar, E. P. 2013, SoPh, 284, 405
Domingo, V., Fleck, B., & Poland, A. I. 1995, SoPh, 162, 1
Dulk, G. A. 1985, ARA&A, 23, 169
Fleishman, G. D. 2006, in Proc. Nobeyama Symp., Solar Physics with the Nobeyama Radioheliograph, ed. K. Shibasaki et al. (NSRO Rep. 1; Nobeyama: Nobeyama Solar Radio Observatory), 51
Fleishman, G. D., Kontar, E. P., Nita, G. M., & Gary, D. E. 2011, ApJL, 731, L19
Fleishman, G. D., Kontar, E. P., Nita, G. M., & Gary, D. E. 2013, ApJ, 768, 190
Fleishman, G. D., & Kuznetsov, A. A. 2010, ApJ, 721, 1127
Fleishman, G. D., & Melnikov, V. F. 2003, ApJ, 587, 823
Fleishman, G. D., Xu, Y., Nita, G. N., & Gary, D. E. 2016, ApJ, 816, 62
Grechnev, V. V., Lesovoi, S. V., Smolkov, G. Y., et al. 2003, SoPh, 216, 239
Guidice, D. A., Cliver, E. W., Barron, W. R., & Kahler, S. 1981, BAAS, 13, 553
Hanaoka, Y. 1997, SoPh, 173, 319
Holman, G. D., Aschwanden, M. J., Aurass, H., et al. 2011, SSRv, 159, 107
Kontar, E. P., & Brown, J. C. 2006, ApJL, 653, L149
Kundu, M. R., Grechnev, V. V., White, S. M., et al. 2009, SoPh, 260, 135
Kundu, M. R., White, S. M., Shibasaki, K., Sakurai, T., & Grechnev, V. V. 2001, ApJ, 547, 1090
Kuznetsov, A. A., & Kontar, E. P. 2015, SoPh, 290, 79
Kuznetsov, A. A., Nita, G. M., & Fleishman, G. D. 2011, ApJ, 742, 87
Lee, J., & Gary, D. E. 2000, ApJ, 543, 457
Lee, J., Gary, D. E., & Shibasaki, K. 2000, ApJ, 531, 1109
Lee, J. W., Gary, D. E., & Zirin, H. 1994, SoPh, 152, 409
Lesovoi, S. V., & Kardapolova, N. N. 2003, SoPh, 216, 225
Lin, R. P., Dennis, B. R., Hurford, G. J., et al. 2002, SoPh, 210, 3
Masuda, S., Shimojo, M., Kawate, T., Ishikawa, S.-n., & Ohno, M. 2013, PASJ, 65, 1
Melnikov, V., Kuznetsov, S., & Morgachev, A. 2014, in COSPAR Meeting 40, 40th COSPAR Scientific Assembly
Melnikov, V. F. 1994, R&QE, 37, 557
Melnikov, V. F., Gary, D. E., & Nita, G. M. 2008, SoPh, 253, 43
Melnikov, V. F., & Magun, A. 1998, SoPh, 178, 153
Melnikov, V. F., Shibasaki, K., & Reznikova, V. E. 2002, ApJL, 580, L185
Nakajima, H., Nishio, M., Enome, S., et al. 1994, IEEEP, 82, 705
Neupert, W. M. 1968, ApJL, 153, L59
Nita, G. M., Fleishman, G. D., Kuznetsov, A. A., Kontar, E. P., & Gary, D. E. 2015, ApJ, 799, 236
Nita, G. M., Gary, D. E., & Lee, J. 2004, ApJ, 605, 528
Pal'shin, V., Charikov, Y. E., Aptekar, R. L., et al. 2014, Ge&Ae, 54, 943
Qiu, J., Gary, D. E., & Fleishman, G. D. 2009, SoPh, 255, 107
Schwartz, R. A., Csillaghy, A., Tolbert, A. K., et al. 2002, SoPh, 210, 165
Somov, B. V., & Syrovatskiĭ, S. I. 1976, SvPhU, 19, 813
Stahli, M., Gary, D. E., & Hurford, G. J. 1989, SoPh, 120, 351
Su, Y., Gan, W. Q., & Li, Y. P. 2008, AdSpR, 41, 988
Sui, L., Holman, G. D., & Dennis, B. R. 2006, ApJL, 645, L157
Sui, L., Holman, G. D., & Dennis, B. R. 2007, ApJ, 670, 862
Torii, C., Tsukiji, Y. S. K., Yoshimi, N., Tanaka, H., & Enome, S. 1979, PRIAN, 26, 129
Veronig, A., Vršnak, B., Dennis, B. R., et al. 2002, A&A, 392, 699
Veronig, A. M., Brown, J. C., Dennis, B. R., et al. 2005, ApJ, 621, 482
Vestrand, W. T., Share, G. H., Murphy, J., et al. 1999, ApJS, 120, 409